HIGHLY EFFICIENT COHERENT RAMAN GENERATION

A Dissertation

by

XIA HUA

Submitted to the Office of Graduate and Professional Studies of
Texas A&M University
in partial fulfillment of the requirements for the degree of

DOCTOR OF PHILOSOPHY

Chair of Committee,	Alexei V. Sokolov
Committee Members,	M. Suhail Zubairy
	George R. Welch
	Philip R. Hemmer
Head of Department,	George R. Welch

August 2014

Major Subject: Physics

ABSTRACT

Coherent Raman generation is widely utilized both in fundamental research and in a variety of applications. Once the coherent molecular motion is established, it results in efficient generation of femtosecond Raman sidebands, allowing synthesis of single-optical-cycle pulses, or, for example, enabling detection of bacterial endospores via coherent Raman spectroscopy.

We explore the utility of Raman coherence in two sets of experiments. In the first part of this work, we generate multi-color optical vortices in a Raman-active crystal $PbWO_4$ using two-color femtosecond laser pulses. We verify that the topological charge transfer among the Raman sidebands obeys the expected orbital angular momentum algebra. In the second part of this work, we explore detection and sensing applications, and achieve further improvement of efficiency by using field enhancement due to surface plasmon resonances in aggregates of gold nanoparticles. By scanning the time delay of the probe pulse, we demonstrate a new vibrational spectroscopic technique called time-resolved surface-enhanced coherent anti-Stokes Raman scattering (tr-SECARS). We demonstrate the application of tr-SECARS by detecting hydrogen-bonded molecular complexes of pyridine with water in the near field of gold nanoparticles. We discuss the discrepancy in SECARS enhancement factors, observed in the experiment and calculated theoretically. To understand this discrepancy, we develop a model and simulate the dependence of SECARS spectra on the position and linewidth of the surface plasmon

resonance. Finally, we propose strategies for increasing experimental enhancement factors towards theoretical predictions.

DEDICATION

To my family

ACKNOWLEDGEMENTS

I spent seven years of study at Texas A&M University, working towards my PhD degree. Although the course work and research here are tough, I still have a wonderful experience during my study here. With lots of help from my professors, my classmates, my colleagues, my friends and my family, I can overcome the difficulty I encountered during my course work, my research and my daily life. Therefore, I'd like to give my sincerely gratitude to all these people for their direct or indirect support, love and patience over the last several years.

I would like to give my special thank to my committee chair, Dr. Alexei V. Sokolov, as my good mentor and my good friend. His solid theoretical background in physics, especially in quantum optics, inspired me a lot. He is always supportive to my research and gives me guidelines when I need them. I also want to thank Dr. Marlan O. Scully. He provides his lab and laser systems for my research use. So that I can have access to the essential part of my research tool: Coherent femtosecond laser system. I also want to thank my committee members: Dr. M. Suhail Zubairy, Dr. George R. Welch and Dr. Philip R. Hemmer. For their constructive suggestions and helpful discussions on my research. I also want to thank my committee members and Dr. Aleksei Zheltikov for reviewing my research proposal and give helpful suggestions.

Next, I would like to thank Dr. Dmitri V. Voronine, Dr. Miaochan Zhi, Dr. Kai Wang and Dr. Alexander M. Sinyukov, for their hands on help on my research project. I want to thank my colleagues Dr. Xi Wang, Dr. Pankaj K. Jha, Dr. Benjamin D. Strycker,

Dr. Matthew M. Springer and Charles W. Ballmann. We did lots of projects together. I learnt a lot from them. I would like to thank my collaborators Dr. Hans Schuessler, Dr. James Strohaber, Dr. Elango Munusamy and Dr. Steven E. Wheeler. They contribute the essential components of this research work. Without them, this research cannot be finished.

At last, but not least, I want to thank all my friends in my life. They make my life much easier during my PhD study. I want to thank my parents for their encouragement and support. I also want to thank my wife Yin Hong, who is a United States registered nurse, for her love, and to my daughter Christina Tzu-Hsin Hua for the happiness she brings to me.

NOMENCLATURE

SpRS	spontaneous Raman scattering
SRS	stimulated Raman scattering
CARS	coherent anti-Stokes Raman scattering
CSRS	coherent Stokes Raman scattering
SERS	surface-enhanced Raman scattering/spectroscopy
SECARS	surface-enhanced coherent anti-Stokes Raman scattering
tr-SECARS	time-resolved SECARS
OV	optical vortice
OAM	orbital angular momentum
TC	topological charge
SHG	second-harmonic generation
SPP	spiral phase plate
OPA	optical parametric amplifier
FROG	frequency-resolved optical gating
FWHM	full-width half maximum
AS	anti-Stokes
THG	third-harmonic generation
FWM	four-wave mixing
SPR	surface plasmon resonance
MPTMS	3-mercaptopropyltrimethoxysilane

TABLE OF CONTENTS

Page

LIST OF FIGURES

Page

LIST OF TABLES

Page

CHAPTER I

INTRODUCTION: FROM SPONTANEOUS RAMAN TO COHERENT SURFACE-ENHANCED RAMAN GENERATION

Raman scattering is a technique that can be used to detect the vibrational, rotational and other low frequency modes in a system. Since the Raman spectrum is unique for each type of molecules, it can be used to identify different molecule types. Therefore, Raman spectroscopy is a powerful tool to detect and identify chemicals. When the chemical amount is small, the Raman signal will be small. People need to increase the Raman efficiency in order to get an increased Raman signal. When the detected amount goes down to a single molecule, the even higher Raman transition efficiency is required. In order to fulfill the requirement of modern applications for highly efficient Raman scattering, new methods are needed.

Raman spectroscopy was discovered and developed by C. V. Raman as a form of spontaneous Raman scattering (SpRS) [1]. As it is a spontaneous process, the signal strength of SpRS is usually very weak. In 1961, people developed stimulated Raman scattering (SRS) [2]. In stimulated Raman scattering, Stokes photons were injected together with the pump photons, or some Stokes photons previously generated by spontaneous Raman scattering were forced to remain in the material. With the presence of the Stokes photons, pump photons were converted more rapidly into additional Stokes photons. Therefore, the rate of Raman-scattering rate was increased. In 1964, coherent anti-Stokes (Stokes) Raman scattering (CARS or CSRS) was developed [3, 4]. CARS is a

third-order nonlinear optical process where a signal photon is produced from three input photons: A pump photon, a Stokes photon and a probe photon. The three input waves interact with the Raman material and generate a coherent optical signal at the anti-Stokes frequency. Because the process is coherent, CARS is orders of magnitude stronger than spontaneous Raman scattering. Also, surface-enhanced Raman spectroscopy or surface-enhanced Raman scattering (SERS) was developed as a surface-sensitive technique that enhances Raman scattering [5-11]. In SERS, Raman molecules are attached to a mental surface. One reason why the enhancement of the Raman signal occurs is because of an enhancement in the electric field provided by the surface. The 10^4-10^{12} enhancement factor of SERS has been observed [5, 10-12], which means SERS is capable to detect single molecules [13-15].

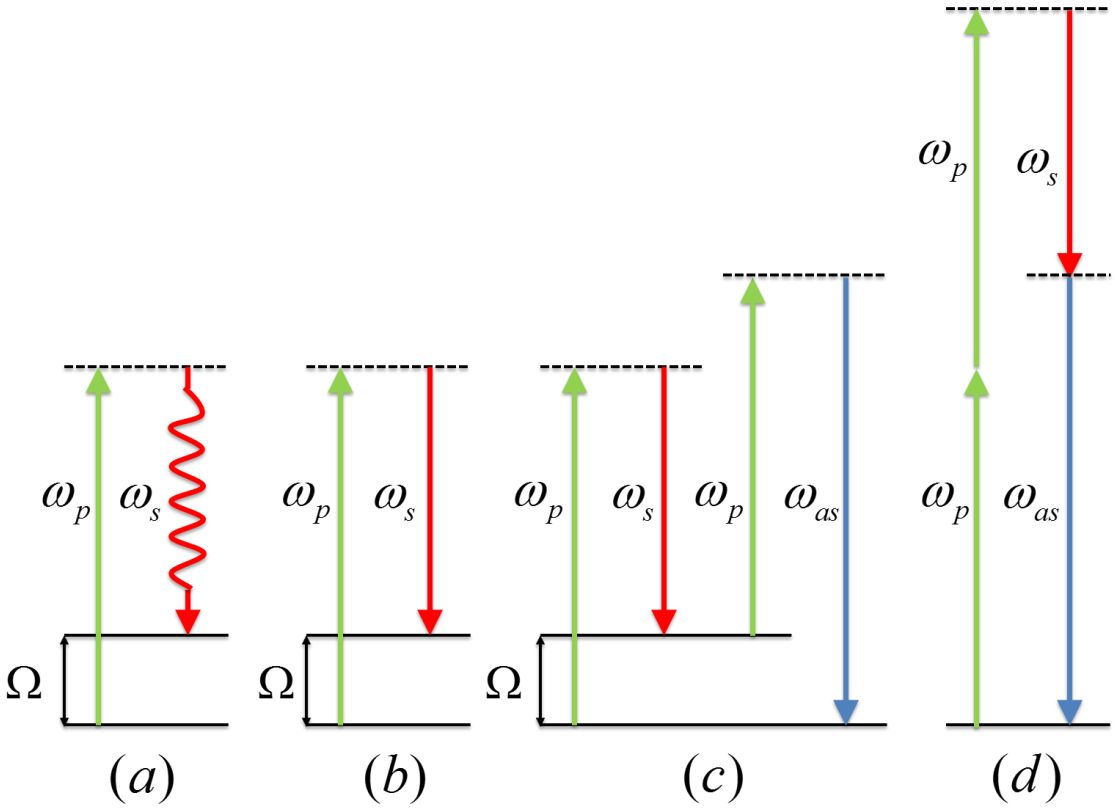

Figure 1 Schematics of (a) spontaneous Raman scattering, (b) stimulated Raman scattering, (c) coherent anti-Stokes Raman scattering, (d) four wave mixing

CHAPTER II

GENERATION OF FEMTOSECOND OPTICAL VORTICES BY MOLECULAR MODULATION IN A RAMAN-ACTIVE CRYSTAL*

In this chapter, we demonstrated an application of coherent anti-Stokes Raman scattering generated in a Raman-active crystal $PbWO_4$. By producing an optical vortex in the pump beam, we generated multi-color optical vortices in a Raman-active crystal $PbWO_4$ using two-color Fourier-transform limited femtosecond laser pulses. This setup overcomes some of the limitation of our previous research by allowing for the production of subcycle femtosecond optical vortices without the need for compensating for added chirp. In addition, the use of an optical parametric amplifier (OPA) allows for greater flexibility in exciting different Raman modes. We verified the topological charges using two different methods. These diagnostic experiments verify not only theoretically predicted OAM algebra but also demonstrated instabilities in high order OVs. We have also studied factors, which affect the high-order vortex sidebands such as the diameter and intensity of the input beams.

*Reprinted with permission from "Generation of femtosecond optical vortices by molecular modulation in a Raman-active crystal" by Miaochan Zhi, Kai Wang, Xia Hua, Hans Schuessler, James Strohaber, and Alexei V. Sokolov, 2013. *Opt. Express,* vol. 21, pp. 27750, Copyright [2013] by The Optical Society of America.

II.A. Introduction

Optical vortices (OVs) are beams of light that carry orbital angular momentum (OAM) and exhibit a singularity point where the intensity is zero and the phase is undetermined. The OV phase structure can be described mathematically by $\exp(il\theta)$, where θ is the azimuthal coordinate, and the integer θ is the so-called azimuthal mode number and is directly related to the topological charge (TC) [16]. Optical vortices have found many applications such as optical tweezers and spanners [17], super resolution spectroscopy [18], light-matter wave interactions in Bose-Einstein condensates [19, 20], communication technologies [21] and nanofabrication [22, 23].

Interaction of OV beams with nonlinear crystals has been studied in the context of parametric frequency conversion processes [24]. Previous experiments demonstrated that the TC of OV beams can exhibit nondestructive conversion during parametric interactions. By using an OV to pump a mid-infrared optical parametric oscillator, Miyamoto et al showed that the TC of the pump laser is selectively transferred to the signal outputs [25]. Optical vortex beams interacting via degenerate two-wave mixing in a Kerr-like nonlinear medium has been investigated experimentally and showed that vortex mixing occurs inside the nonlinear medium, which leads to exchange of topological charge and cascaded generation of vortex beams [26]. Second-harmonic generation (SHG) with vortex beams has also been investigated for two decades; it was found that each mode becomes doubled in frequency and transformed into a higher order vortex mode [27]. Recently, SHG of

fractionally-charged OV beams has been studied with femtosecond radiation [28]. The OAM of the generated second harmonic field is always zero and is independent on the displacement of the spiral phase plate (SPP), which is used to generate the OV beam. How femtosecond OV beams interact within a Raman crystal has not yet been fully explored. This is an interesting subject in that femtosecond OVs is a relatively new area [29-31].

We wish to extend upon our group's previous work by studying the interaction of femtosecond OVs in a Raman active crystal with the goal of spatio-temporally engineering subcycle optical pulses [32-34]. Our group have studied coherent transfer of OAM in multi-order Raman sidebands [35] using a pair of linearly chirped pulses (hundreds of femtoseconds in duration), which allowed to excite the Raman mode at 320 cm^{-1}. However, because this is a coherent process, the output beams are chirped, and a compensator is required to achieve subcycle pulses [36]. One method to overcome this difficulty is to use a two-colored femtosecond scheme employing an OPA. In addition, by using a pair of femtosecond pumping laser pulses from an OPA, we can efficiently access the high gain, high frequency Raman mode of $PbWO_4$ at 901 cm^{-1}. In our earlier experiment, our pump and Stokes beams had either the same charge $l_p = l_s = |l|$ or opposite charges $l_p = -l_s = |l|$ with $|l| = 1$. In the current work, we shape each beam independently with the pump and Stokes beam having TCs of $|l| = 1$ and 0 respectively. This is an interesting situation because it has been predicted by theoretical calculations that the resulting OVs generated in a Raman medium will have incremental increases of charge 1 from one Raman sideband to the next according to the relationship

$l_n = l_p + n(l_p - l_s)$. The pairwise sum of the TCs in the n^{th} order AS and S is equal to the sum of the TCs in the pump and Stokes, i.e. $l_p + l_s = l_n + l_{-(n+1)}$ [35, 37]. For example, when $l_p = 1, l_s = 0$, for $n = 5$, the mode number of AS5 is $l_5 = 6$ and for S5, the mode number is $l_{-6} = -5$. When coherently super-imposing the OVs both spatially and temporally, helical beams can be formed, which allow us to verify another case of the OAM algebra [35, 37].

II.B. Experimental setup

The experimental setup is shown in Figure 2. We used a Ti:sapphire amplifier, which outputs 40 fs pulses with center wavelength at 806 nm and having a 1 kHz repetition rate. Part of the beam was used as the pump beam for Raman generation while the other part was used to pump an optical parametric amplifier (OPA). The second harmonic (870 nm) of the idler beam from the OPA was used as the Stokes beam (Here we follow the coherent anti-Stokes Raman scattering convention and denote the shorter 806 nm wavelength beam as pump and the long wavelength 870 nm as the Stokes beam.). We

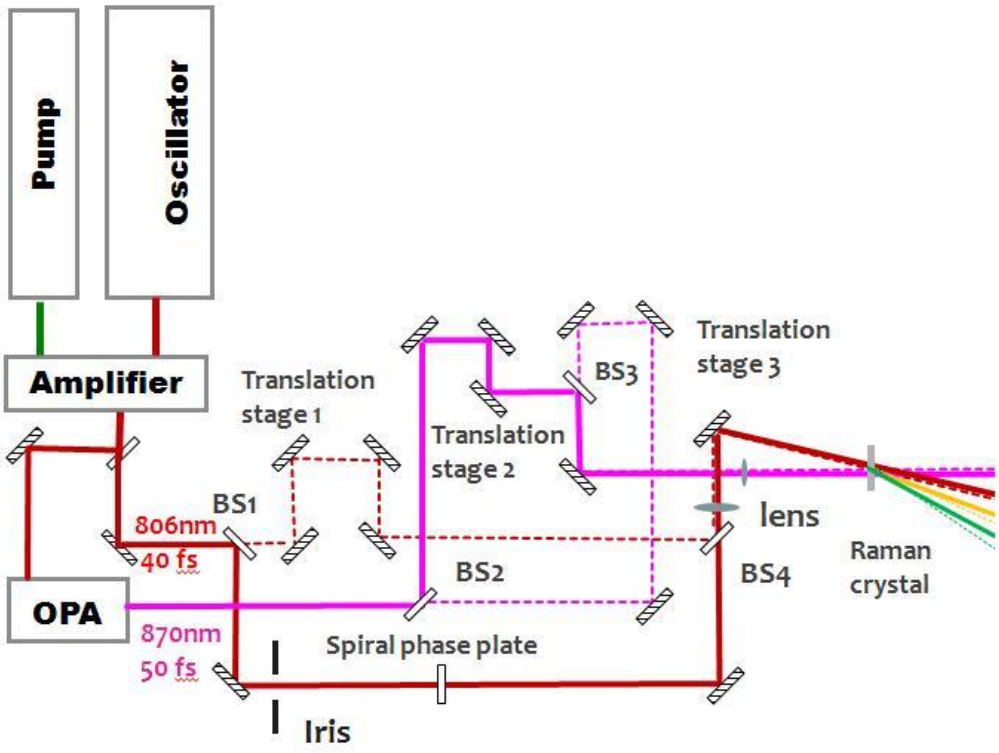

Figure 2 Schematics of the femto-second vortices generation experimental layout.

label the sidebands as anti-Stokes one (AS1), anti-Stokes two (AS2), and so on. A typical spectrum measurement of a single sideband generated in the coherent Raman process had been shown in Figure 3. A frequency resolved optical gating (FROG) measurement had been shown in Figure 4 (The sideband is generated in diamond). This showed that, in principle, using femtosecond pulses, we could generate the coherent sidebands in the femtosecond region [38, 39]. In order to perform interferometric experiments, both the

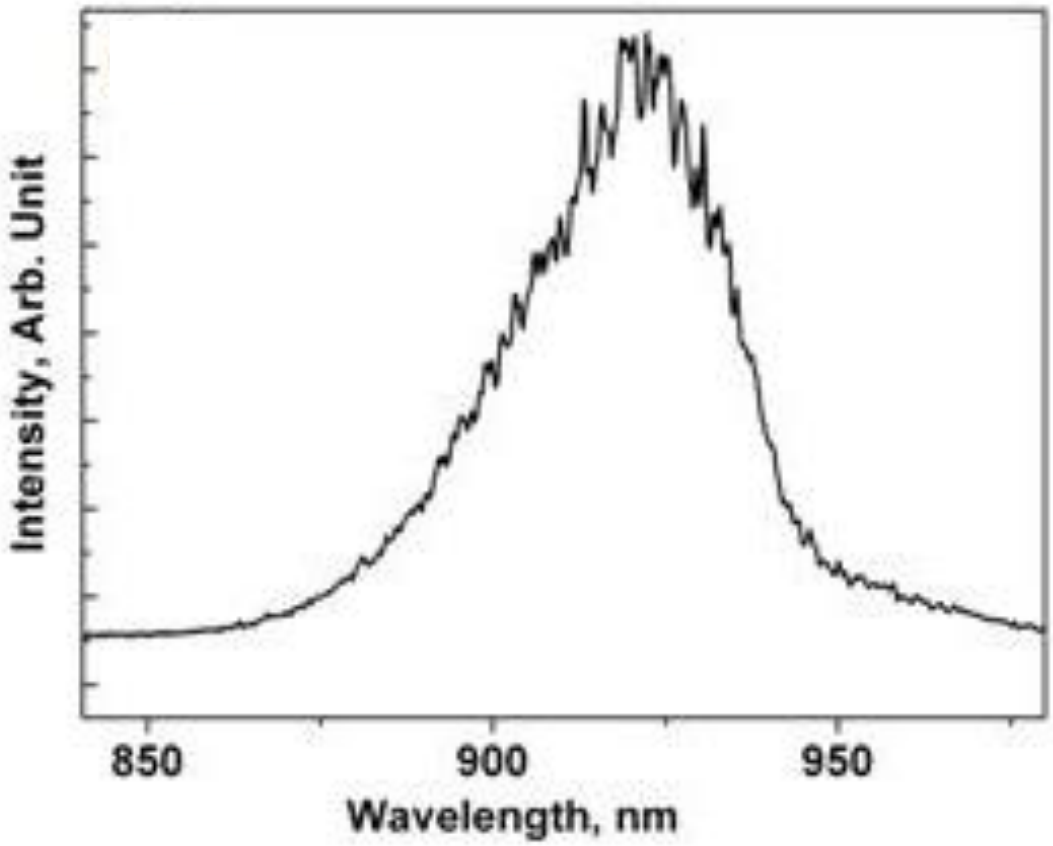

Figure 3 The typical spectrum measurement of AS1 generated from Raman crystal (diamond). The center wavelength is at 940 nm.

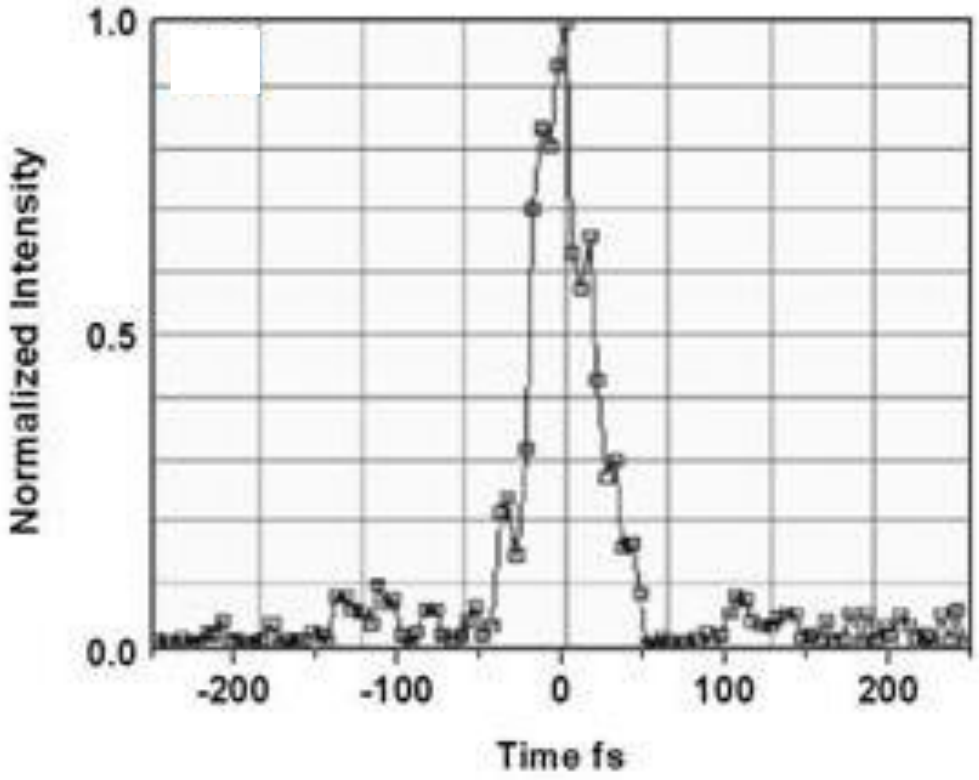

Figure 4 The typical FROG measurement of AS1 generated from Raman crystal (diamond), performed using Phazzler (FastLite). The dispersion of the pulse has been corrected by Phazzler. The full-width half maximum (FWHM) is measured to be 32.8 fs.

pump and the Stokes beams were split into two so that a reference set of Raman sideband could be generated in a 0.5 mm thick Raman crystal $PbWO_4$ (shown as the solid and dotted lines in Figure 2). The solid-lined pair was used to generate the femtosecond OVs in the Raman sidebands. The pump beam, shaped by a spiral phase plate having an azimuthal structure divided into 16 segments with each step contributing $n\pi/8$ phase shift

[40], contained an OV of $l = \pm 1$. The other pair of beams (dotted line) was used to generate the reference sidebands with Gaussian profile $l_n = 0$. The power of each pump beam is around 5 mW and the power of each Stokes is around 0.5 mW. The power of AS1 is around 0.5 mW.

In theory, the center wavelength of the sidebands could be determined by $\omega_n = \omega_p + n\omega_R$, where ω_R is the angular frequency of the Raman mode and ω_n is the center angular frequency of the Raman sideband. In experiments, the frequency spacing between the sidebands decreases gradually for the higher sidebands [34, 41]. Three translation stages were used to control the relative delay between the pump and Stokes beams of each pair, and to add an overall delay between the reference and OV sidebands.

II.C. Femtosecond optical vortex generation in a $PbWO_4$ Raman-active crystal

In previous experiments, research has been done on the coherent transfer of optical OAM to the sidebands from the pump and Stokes beams [35]. This transfer was observed in the first three orders and was in agreement with predictions. In order to investigate this transfer into the higher orders, improvements to the beam quality were needed. For this reason, we explored ways to produce high quality OV beams in the sidebands. For all experiments, the input beams had a few mW of power and were focused by a lens with a nominal focal length of 30 cm. The angle between the pump and Stokes beams was about 4 degrees so that phase matching conditions could be satisfied. This is important because phase matching plays an important role in broadband light generation using solids [34]. In

order to produce high fidelity ultrashort optical vortices in the sidebands and to accurately measure TCs, high fidelity input OV beams are necessary. For this reason, The SPP was adjusted until highly symmetric doughnut-shaped beams were produced. In addition, much care was taken to align the temporal and spatial overlaps, and to adjust the relative size of the pump and Stokes beams.

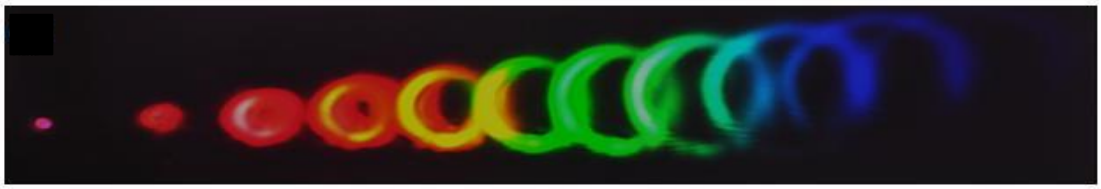

Figure 5 Different diameter of OVs generated in a Raman crystal by controlling the intensity and the beam diameter. OVs are overlapped because the divergence of OV is bigger than the separation angle between two sidebands.

The results of our first experiment are shown in Figure 5. Up to 8 ring-shaped sidebands were observed, however, these sidebands overlap making it impossible to independently manipulate their phases/amplitudes or measure the TC. Because the divergence of Laguerre Gaussian beams depends inversely on the beam waist $\theta \sim \lambda / w_0$ and because the waist is inversely related to the beams size w_L at the lens $w_0 \sim \lambda f / w_L$, the divergence of the beams are proportional to the beams size at the lens $\theta \sim w_L / f$. Therefore, to separate the OV sidebands, we controlled their divergence by adjusting the iris before

the lens in our setup. Figure 6 shows the result of the separate OV beams up to the tenth order as a consequence of reducing their divergence angle.

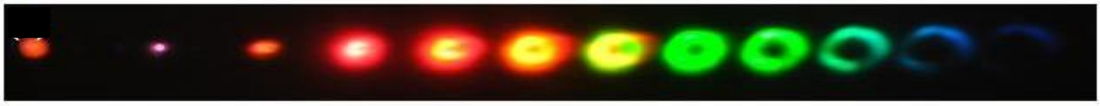

Figure 6 Decreasing the beam waist with iris before SPP to reduce the divergence. OVs are separated.

Pulse energy is another important factor, and it must be managed because higher pulse energies lead to nonlinear effects such as self-focusing resulting in sideband distorted. To demonstrate this, we show an image of OVs generated at different power levels. The maximum power of each pump beam is around 5 mW. The intensity for the pump beam on the crystal is around 10^{11} W/cm^2. The maximum power of the Stokes beam is around 0.5 mW. The intensity for the Stokes beam on the crystal is around 10^{10} W/cm^2. The OVs Figure 5 and Figure 6 were generated with more pulse energy. The OVs displayed in Figure 7 were measured at a decreased beam power. Although only a

Figure 7 Adjusting the power of pump and Stokes. When the intensity of the pump and Stokes beams are attenuated, low-order sidebands OVs have symmetric beam profiles; OV are ready to be measured.

few sideband OVs are generated, the intensity is more uniform across the rings than those shown in Figure 5 and Figure 6 taken at higher pulse energies. Figure 8 shows the beam profiles of AS1 to AS8 after adjust both beam waist and power of pump and Stokes.

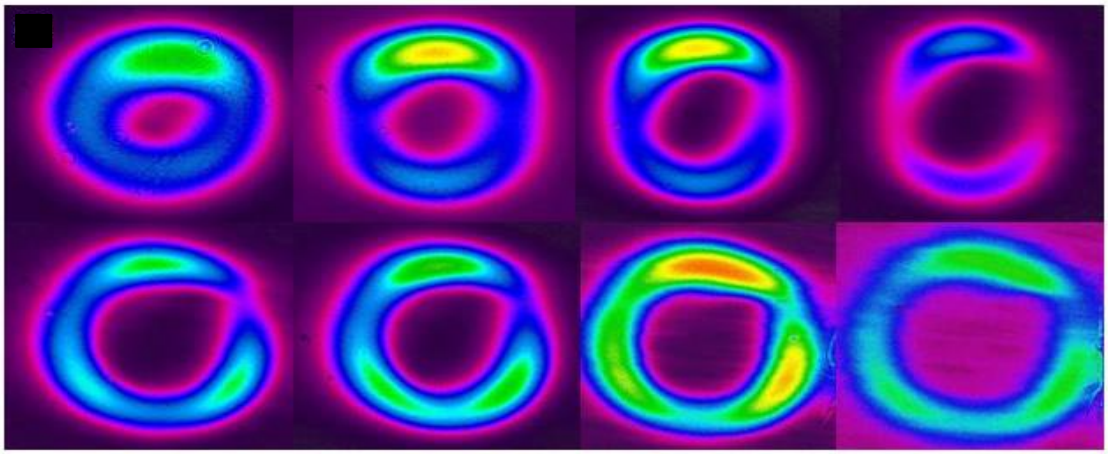

Figure 8 The beam profiles of AS1 to AS4 (Top, from left to right) and AS5 to AS8 (Bottom, from left to right).

II.D. Topological charge measurement

II.D.1. Method one: using a tilted convex lens

Various methods have been proposed to measure the topological charge of OVs such as annular and triangular apertures [42, 43]. Here we first measure the TC of our Raman sidebands by a simple method, which has been recently proposed —a tilted convex lens [44]. By tilting a lens to a tangent angle of about 6 degrees and recording the intensity distribution of a propagating vortex at the focus, the sign and magnitude of the OV can be determined. As an example, we can measure the TC by counting the nodes of the beam profiles at the focus shown in the middle column of Figure 9, Figure 10 and Figure 11. We used low power for the pump and Stokes beams so that only a few sidebands were generated, which corresponds to the low power situation in Figure 7. The results of the OV charge measurements are shown in Figure 9, Figure 10 and Figure 11.

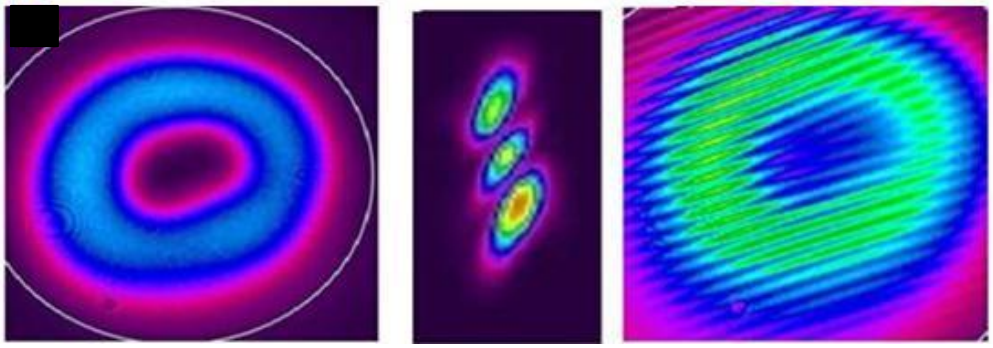

Figure 9. OV sidebands AS1 topological charge measurement using a tilted lens. From left to right are the OV before the lens, after the lens and interference with a Gaussian reference beam.

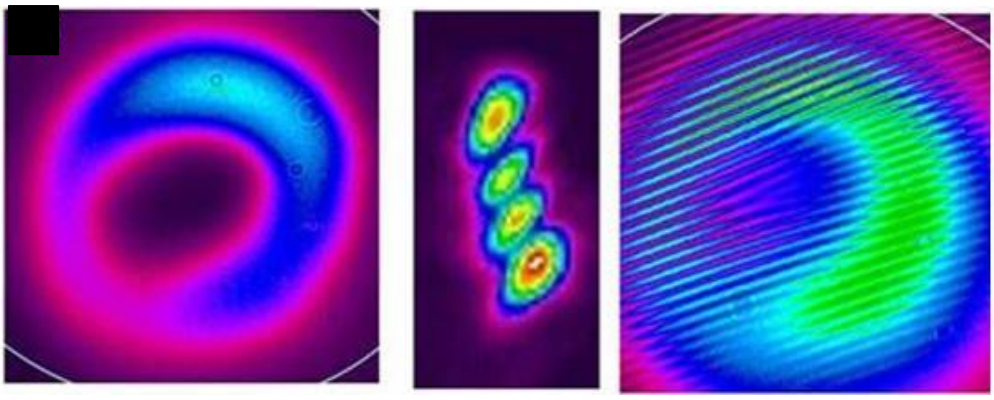

Figure 10. OV sidebands AS2 topological charge measurement using a tilted lens. From left to right are the OV before the lens, after the lens and interference with a Gaussian reference beam.

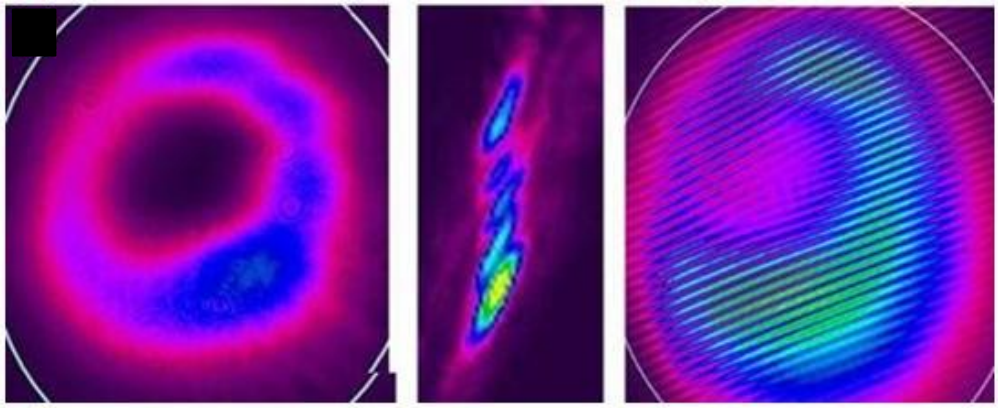

Figure 11 OV sidebands AS3 topological charge measurement using a tilted lens. From left to right are the OVs before the lens, after the lens and interference with a Gaussian reference beam.

II.D.2. Method two: using an interferometer scheme

The tilted lens method does give a quick check of the TC of the sidebands; however, to obtain detailed phase information, we find that the interferometer is the best method [35]. To this end, we have split the pump and Stokes beams into two. The first pair of beams (solid lines in Figure 2) has relatively more power and was focused on the bottom bright spot on the crystal, while the second pair was focused on the top spot on the crystal, as shown schematically in Figure 12. As mentioned above, the pump beam in the first pair was shaped by a spiral phase plate and had a TC of 1. When the pump and Stokes in each pair of beams were spatially and temporally overlapped, we realized generation of many order of Raman sidebands. By adjusting the temporal delay between the two pairs of beams, Young's interference experiment was simultaneously realized for each sideband. These OV-containing sidebands have a larger diameter and were partially overlapped with the sidebands that were generated by the Gaussian reference pair. The interference between the two sets of sidebands is used to determine the helicity and topological charge in each order. In Figure 12, we show the common straight fringe

Figure 12 Two pairs of beams are focused in different part of a Raman-active crystal—$PbWO_4$. The beams are close and overlap partially. The interference of the beams occurs and gives the phase profiles of the optical vortices.

pattern for the Stokes beam, which has OAM of 0, and a typical fork pattern, which results from the interference of two pump beams with l=0 and 1 respectively. We have found that the OAM is transferred to the higher anti-Stokes orders according to $\ell_n = \ell_p + n(\ell_p - \ell_s)$. By using interference, the TCs of the anti-Stokes (AS) Raman sidebands were measured up to 3 orders for low power pumps, as shown in Figure 9 to Figure 11. The interference fringes of the Raman sideband orders up to AS3 are consistent with that expected from the OAM algebra. To observe the interference of AS4 and AS5 orders, more pump and Stokes pulse energy was needed. In Figure 13, we show the AS1 to AS5 OV sidebands charge measurements using slightly higher powers of the pump beams. The interference pattern of the AS orders AS1—AS3 are similar to the low power situation although the OV shapes become slightly distorted (less symmetric) possibly due to other nonlinear processes such as self-focusing. For high-order sideband such as AS4 and AS5 we used

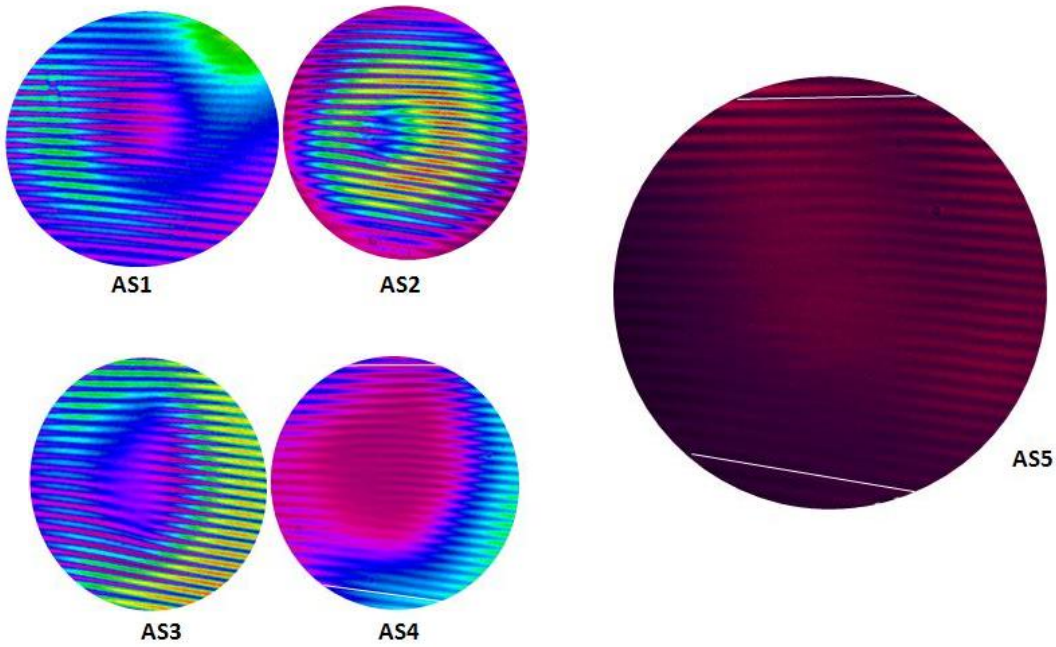

Figure 13 Interference patterns of the Raman sidebands orders AS1 to AS5.

higher pulse energies in addition to an iris which was used to cut the high intensity ring and focus on the dark core region (Figure 13). In between the two white lines on the interference phase map of AS4, there are 20 bright fringes on the left side and 25 on the right side. This indicates that the TC is 5. Similarly for AS5, on the left there are 20 constructive interference fringes while on the right side there are 26, which give the measurement TC of 6. We also measured the spectrum of the AS11 OV (Figure 14) with a Gaussian spectrum fit that is centered on 479 nm. The spectral profile is Gaussian, and is capable of supporting a Fourier-transform-limited pulse duration of 68 fs.

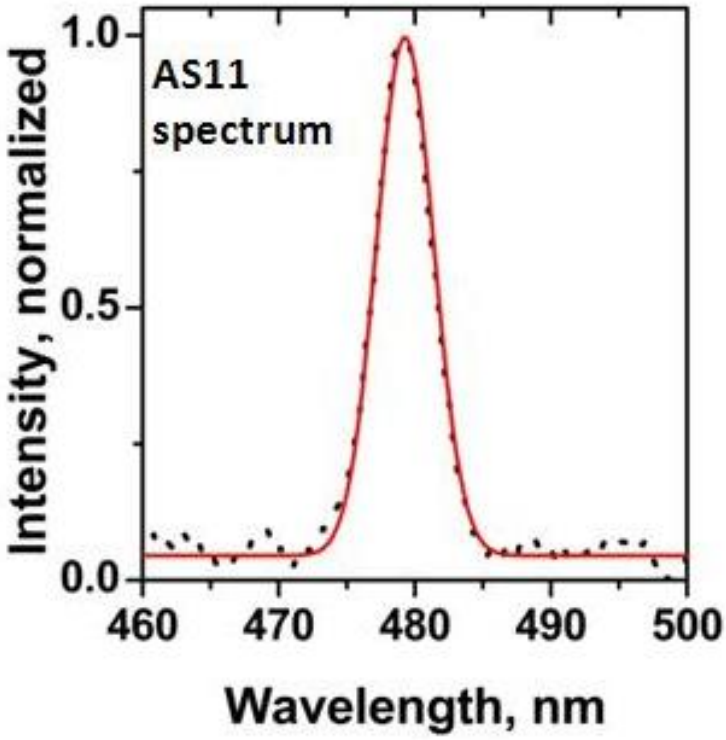

Figure 14 The spectrum of the AS11 OV (black dotted line) with a Gaussian spectrum (red line) fit that is centered on 479nm. This spectral profile is Gaussian, and is capable of supporting a Fourier-transform-limited pulse duration of 68 fs.

Instead of the expected general multifurcation for TC of order $\ell > 1$, where the singularity is at a single point, we observed splitting of the multifurcation into several smaller multifurcations when both low and high energy pump and Stokes pulses were used. The sums of the bifurcations/multifurcations will give us the mode number l_n. When we moved the beam profiler along the beam propagation direction of the beams we

observed stable fringes. We therefore concluded that this splitting occurs with high-energy femtosecond pulses, and we suspected that the splitting may have occurred inside the Raman crystal following generation. This is highly probable as it is well-known that high order vortices $|\ell| > 1$ are unstable and split into several charge 1 vortices [45]. We speculate that by using a thinner crystal, we may be able to avoid such splitting and further increase the fidelity of these beams. Although we are not able to measure the topological charge of the sidebands beyond AS5, the donut-like sidebands can be seen up to 8th order with increasing diameter (Figure 5 and Figure 6). This increase is an indication of the presence of high-order OAM [35].

II.E. Conclusion

We have generated many orders of multi-color OV beams by focusing an OAM containing pump beam and a femtosecond Stokes beams into a Raman-active crystals. We have shown that the OVs are sensitive to the pulse energy, beam diameter as well as the spatial-temporal overlaps of the beam. We used two methods—a tilted lens and an interferometer to measure the TC of the OVs and found that the generated OVs follow OAM transfer in a way similar to frequency conversion. The interference fringes of the OV beams and Gaussian reference beam show that the high-order OVs generated inside Raman crystals are unstable and split in to several charge 1 OVs. In a previous experiment using a nearly identical setup, we measured the coherent Raman sidebands generated in diamond [36, 39]. This previous work showed that with the assistance of a pulse shaper

and prism, we could synthesize ultrafast waveform using the first five Raman sidebands covering the spectral range from 752 nm to 580 nm. These vortices, in principle, could support a 3.5 fs vortex beam, if spatially and temporally combined with proper phases.

CHAPTER III

TIME-RESOLVED SURFACE ENHANCED COHERENT SENSING OF NANOSCALE MOLECULAR COMPLEXES*

In chapter two, we demonstrated an application of coherent anti-Stokes Raman generation in a way that generating femtosecond optical vortices in a Raman active crystal, with the goal of spatio-temporally engineering subcycle optical pulses. CARS is orders of magnitude stronger than spontaneous Raman scattering because of it's a coherent process. But some Raman applications requires even larger enhancement of Raman signals. In this chapter, we will study the nanoscale real-time molecular sensing using Raman technique, which requires large signal enhancement, small background, short detection time and high spectral resolution. We demonstrate a new vibrational spectroscopic technique, which satisfies all of these conditions. This time-resolved surface-enhanced coherent anti-Stokes Raman scattering (tr-SECARS) spectroscopy is used to detect hydrogen-bonded molecular complexes of pyridine with water in the near field of gold nanoparticles with large signal enhancement and a fraction of a second collection time. Optimal spectral width and time delays of ultrashort laser pulses suppress the surface-enhanced non-resonant background. Time-resolved signals increase the spectral resolution, which is limited by the width of the probe pulse and allow measuring nanoscale vibrational

*Reprinted with permission from "Time-Resolved Surface-Enhanced Coherent Sensing of Nanoscale Molecular Complexes" by Dmitri V. Voronie, Alexander M. Sinyukov, Xia Hua, Kai Wang, Pankaj K. Jha, Elango Munusamy, Steven E. Wheeler, George Welch, Alexei V. Sokolov and Marlan O. Scully, 2012. *Scientific Reports,* vol. 2, pp. 891, DOI: 10.1038/srep00891, Copyright [2012] by Nature Publishing Group.

dephasing dynamics. This technique combined with quantum chemistry simulations may be used for the investigation of complex mixtures at the nanoscale and surface environment of artificial nanostructures and biological systems.

III.A. Introduction

Detecting molecular complexes at the nanoscale presents a challenge for current state-of-the-art spectroscopy due to weak signals from small amounts of material, spectral congestion from complex mixtures and background from solvents, substrates or the molecules themselves. Two of the most commonly used techniques that provide species-specific spectroscopic signals in the form of vibrational fingerprints are surface-enhanced Raman scattering (SERS) [5, 6, 10, 11] and coherent anti-Stokes Raman scattering (CARS) [46] spectroscopies. In order to enhance the signal by several orders of magnitude, SERS takes advantage of the electromagnetic near-field enhancement while CARS employs molecular coherence. Several attempts have been previously made to combine these two techniques to achieve best-of-both-worlds maximum signal enhancement [13, 47-53]. However, small enhancement factors, low spectral resolution, large background and poor reproducibility have limited application of these implementations. Overcoming these difficulties may lead to significant improvements in nanoscale sensing and new breakthrough applications in real-time label-free nano-imaging of biomolecules, detection of toxic chemicals and hazardous materials, genome sequencing, nano-catalysis and many others.

Here we have mitigated these drawbacks and demonstrated a new combination of surface and coherence enhancements by using laser pulse shaping and time-resolved detection. We applied this new time-resolved surface-enhanced coherent anti-Stokes Raman scattering (tr-SECARS) technique to investigate molecular complexes of pyridine in the vicinity of gold nanoparticles. Various molecular complexes can be formed by interaction with a nitrogen atom of pyridine (Figure 15). Hydrogen-bonded

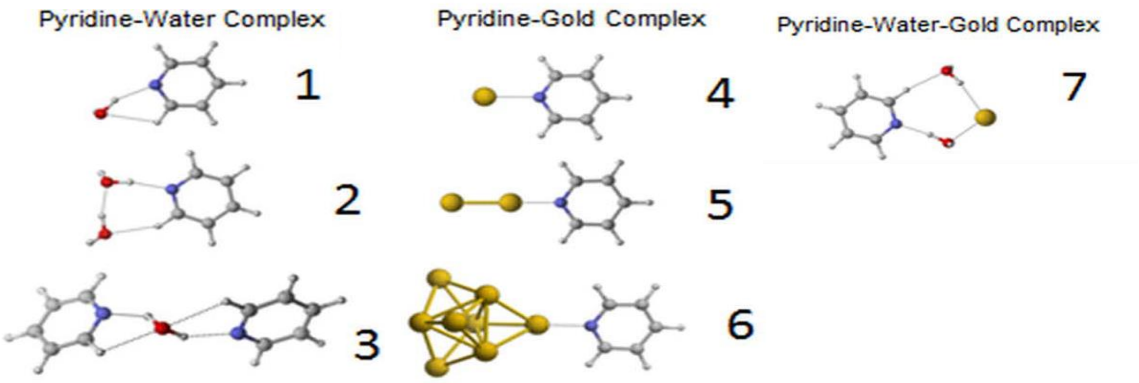

Figure 15 Equilibrium structures of various pyridine, water and gold complexes obtained from quantum chemical DFT calculations. Time-resolved SECARS identified structure 1 as the dominant species.

complexes with water cannot be excluded as water may be present in small amounts on the surface of gold. Pyridine-water complexes have been previously studied using Raman spectroscopy [54-56], and pyridine was the first molecule for which SERS was

demonstrated [6]. Single molecules and monolayers are usually the targets of research and proof-of-principle demonstrations. However, the ultimate goal is often to detect multilayer nanomolar amounts of chemicals. The near-field of plasmonic nanoparticles decays exponentially extending into a few layers of covering molecules (Figure 16). If these molecules are excited coherently, they may provide strong signal enhancement even from a small volume. The signal then originates both from molecular surface species and environment (including the native resonant bands of the bulk pyridine) in the vicinity of nanoparticles.

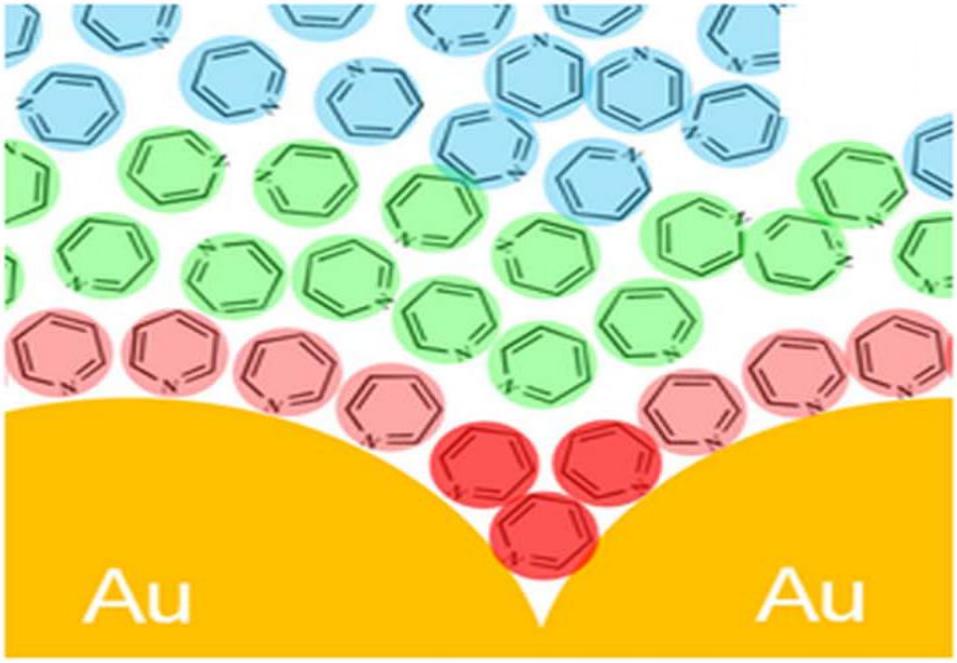

Figure 16 Model of pyridine molecules directly attached to (red) and in the vicinity of (green) gold nanoparticles. Bulk pyridine molecules far from the surface show no signal enhancement (blue).

III.B. Sample preparation and characterization

III.B.1. Synthesis of gold nanoparticles

We used a modified procedure that was previously reported to produce random aggregated gold nanoparticles (NPs) on glass substrates[47, 57]. The synthesis of colloidal gold NPs was performed by reduction of HAuCl4 with sodium citrate[47, 57, 58]: 100 ml of 0.1 mM aqueous solution of HAuCl4 was stirred and heated until boiling. Then 10 ml of 0.4 mM aqueous solution of trisodium citrate was added. As a result, individual spherical gold NPs 10-15 nm in diameter were obtained (Figure 17).

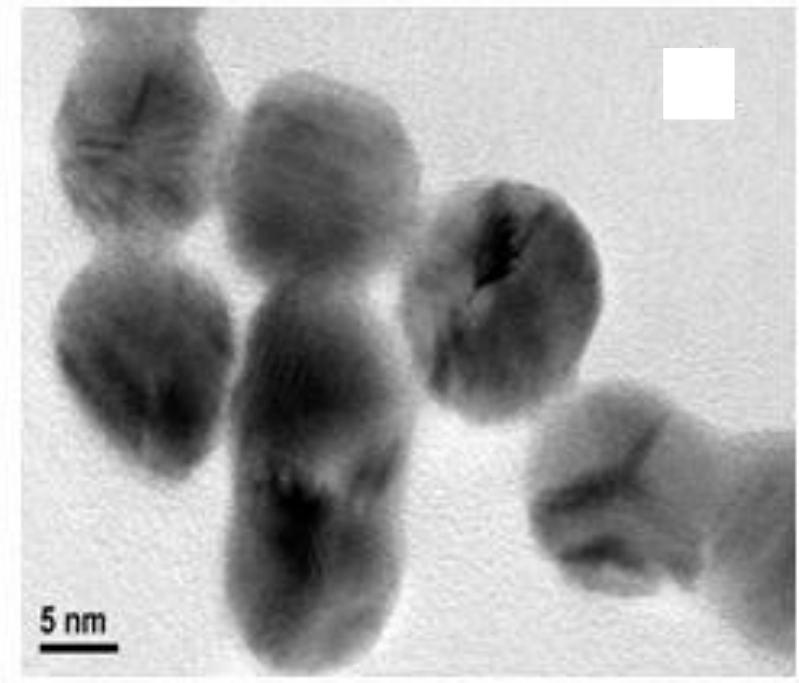

Figure 17 TEM image of individual gold nanoparticles (NPs).

III.B.2. Preparation and characterization of substrates

Microscope slides were cleaned using concentrated sulfuric acid (98%) overnight, trichloroethylene (30 min), acetone (30 min), and methanol (30 min). All the steps were performed at room temperature. Distilled water was used to rinse the substrates. The glass

slides were derivatized with 3-mercaptopropyltrimethoxysilane (MPTMS). Clean glass slides were kept in a 5% MPTMS solution in methanol for 24 hours[57]. After derivatization, the slides were cleaned with methanol and rinsed with distilled water. Then the gold colloid was deposited onto the surface, covering the whole substrate. After approximately 2 hours, a uniform layer of aggregated gold NPs on glass substrates was formed.

The obtained nanostructures were characterized by Atomic Force Microscopy (AFM). The resolution of the instrument (MV 4000, Nanonics Imaging) was ~50 nm in the x-y-directions and ~0.2 nm in the z-direction. A typical AFM image is shown in Fig. 17A. Random aggregated nanostructures with a surface roughness of 10 - 200 nm were observed (Figure 18B and Figure 18C). This surface roughness is necessary for surface plasmon excitation to support a large range of frequencies.

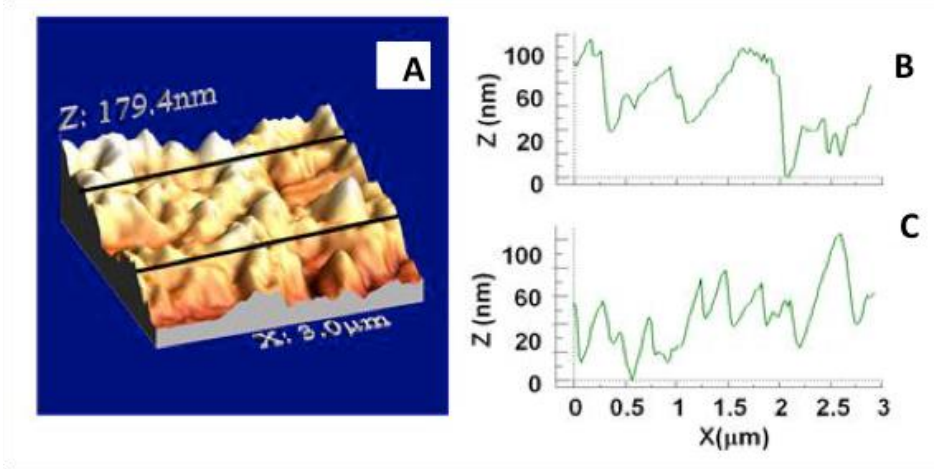

Figure 18 (A) AFM image of random aggregated gold NPs on a glass substrate. (B) and (C) are surface profiles for black lines in A.

III.C. Experimental setup

The experimental setup (Figure 19) is based on a Ti:Sapphire regenerative amplifier (Coherent Legend, 1 kHz rep. rate, 1 mJ/pulse) and was described earlier [59, 60]. Briefly, the pump and Stokes pulses at 560 and 600 nm, respectively, are generated in two evenly pumped optical parametric amplifiers (OPAs), Coherent OPerA-VIS/UV and OPerA-SFG/UV. The probe pulse is directed through a homemade pulse shaper consisting of a pair of gratings to expand the spectrum in space and an adjustable slit at the Fourier plane to pick a narrow spectral band. The probe pulse was shaped by the slit to have a top-hat-like spectrum corresponding to a Sinc-shaped temporal profile (right inset in Figure 19) with a variable width at ~ 805 nm. The temporal delay of each pulse is controlled by an independent translation stage. All three incident beams are collimated

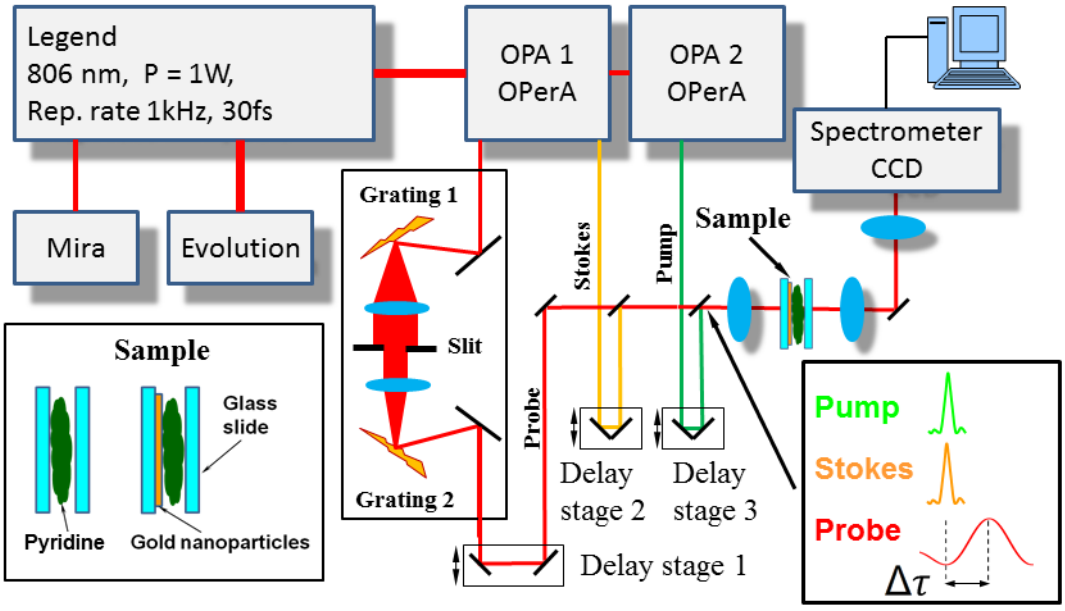

Figure 19 Experimental setup for tr-SECARS. Right inset: laser pulse shapes and a probe delay $\Delta\tau$. Left inset: two types of pyridine samples with and without aggregated gold nanoparticles.

using beam splitters and are collinearly incident on a sample. After transmission through the sample these beams are filtered out and the tr-SECARS signal is recorded with a liquid-nitrogen cooled spectrometer (Andor). Two-dimensional spectrograms are obtained by scanning the time delay of the probe pulse and by recording a spectrum at each step. This optimized time-resolved CARS technique combines the advantages of a uniform coherent excitation of a broad vibrational molecular spectrum by a pair of femtosecond broadband pump and Stokes pulses and a subsequent probing of this prepared molecular coherence

with an optimally shaped picosecond narrowband probe pulse providing high spectral resolution.

III.D. Experimental data

A typical SERS spectrum of pyridine on aggregated gold nanoparticles is shown in Figure 20 (red circles). The observed two strong peaks at 990 and 1030 cm^{-1} correspond to the ring breathing (ν_1) and triangle (ν_{12}) modes, respectively. These modes have been previously observed in SERS spectra on silver and gold colloid nanoparticles[61, 62], aggregates[14] and rough surfaces[6]. We used a 0.2 W Nd:YAG laser beam at 532 nm with 80 sec signal collection time. A similar spectrum was obtained from bulk pyridine without gold NPs with resolution ~ 3 cm^{-1}. Our results agree with the previous reports. We used a modified sample preparation procedure, described in sample preparation part. Briefly, a solution of colloid gold nanoparticles (NPs) with an average diameter, 10 nm (Figure 17) was prepared and then deposited onto a clean glass substrate to form a multilayer aggregate of gold NPs. The resulting surface had a roughness ~ 100 nm as shown in Figure 18. The extinction spectrum revealed a red shift and broadening of the

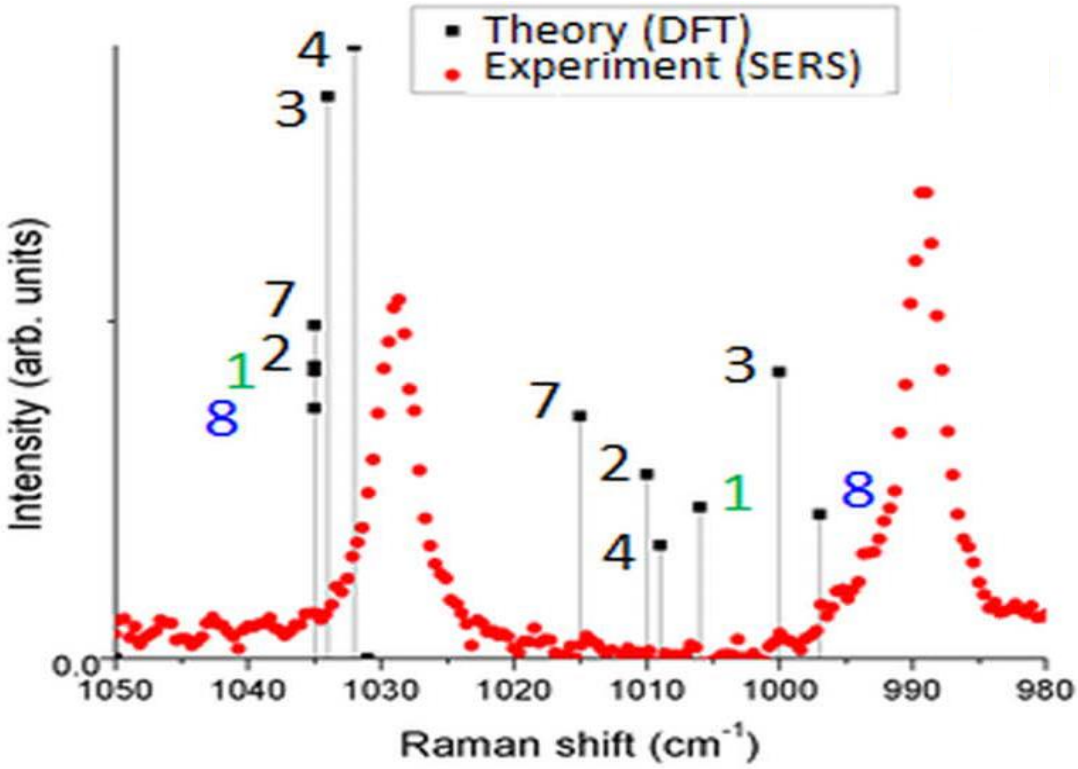

Figure 20 Experimental SERS spectrum of pyridine on the surface of aggregated gold nanoparticles (red circles) and calculated Raman activities of various complexes (thin black lines) corresponding to equilibrium structures shown in Fig. 14. Lines number 8 correspond to simulated signals from pure pyridine.

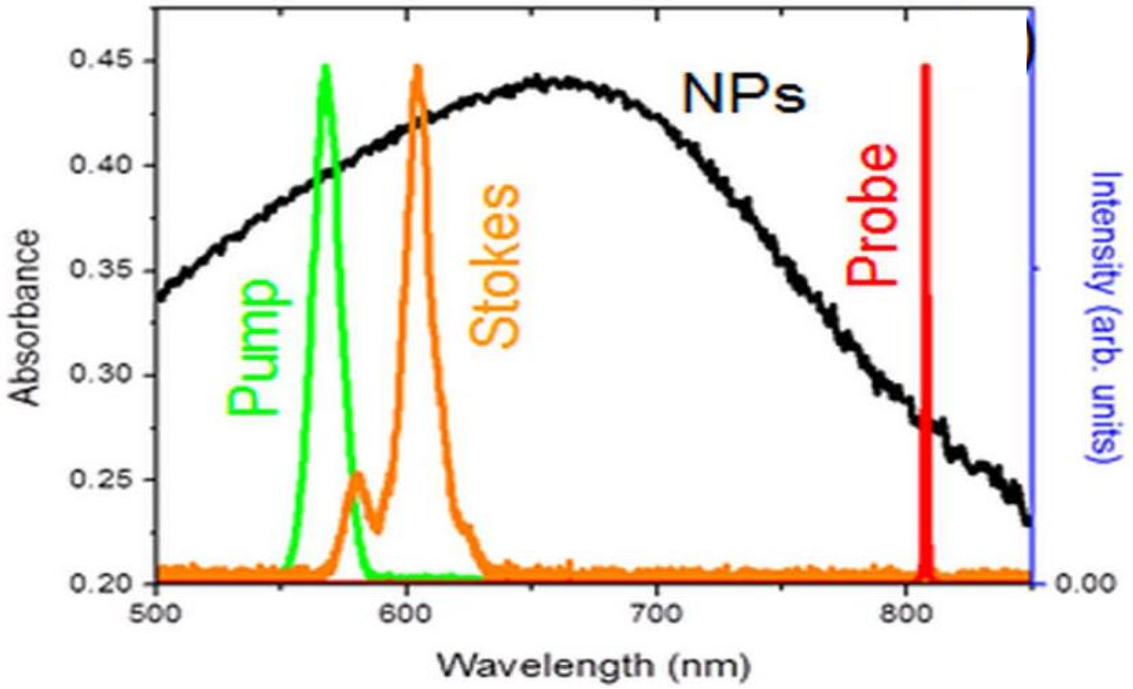

Figure 21 Absorbance spectrum of the gold surface (black, NPs) overlapping with the laser pulse spectra (pump, Stokes and probe) used in the tr-SECARS experiments.

plasmon resonance due to surface aggregation (Figure 21, black line). Similar randomly aggregated nanoparticles have been previously used as SERS substrates[11]. A drop of neat pyridine was deposited onto a gold surface and covered by a microscope glass slide to suppress evaporation. A $12\mu m$ thickness of the pyridine layer between the glass slide and the substrate was measured using an optical microscope. All experiments were performed at room temperature under ambient conditions.

To increase the signal enhancement and to decrease the collection time we implemented a time-resolved surface-enhanced CARS (tr-SECARS) spectroscopy. In contrast to previous femtosecond SECARS techniques, our approach employs femtosecond broadband pump and Stokes pulses to excite molecular vibrational coherence and a picosecond narrowband probe pulse to generate the signal. It is based on our previously developed FAST-CARS approach to suppress the nonresonant background[59, 60, 63]. Here we combine the coherence enhancement of FAST-CARS with the surface enhancement of SERS. This background suppression is essential because plasmonic nanoparticles also enhance the unwanted nonresonant four-wave mixing. This has been a challenge of several recent experiments on surface-enhanced CARS spectroscopy[48, 49, 52]. The combination of these advantages allows the use of tr-SECARS to detect and investigate molecular species adsorbed onto the surface of nanoparticles in the presence of the background bulk molecules not interacting with the surface.

We performed tr-SECARS spectroscopy of the $12\mu m$ thick pyridine samples described above. The experimental setup is based on the previously described configuration [59, 60]. A simplified scheme in Figure 22 shows three collinear laser pulses incident on a sample of gold nanoparticles coupled to pyridine molecules. The full setup is described in the Experimental Setup section. Briefly, the center frequencies

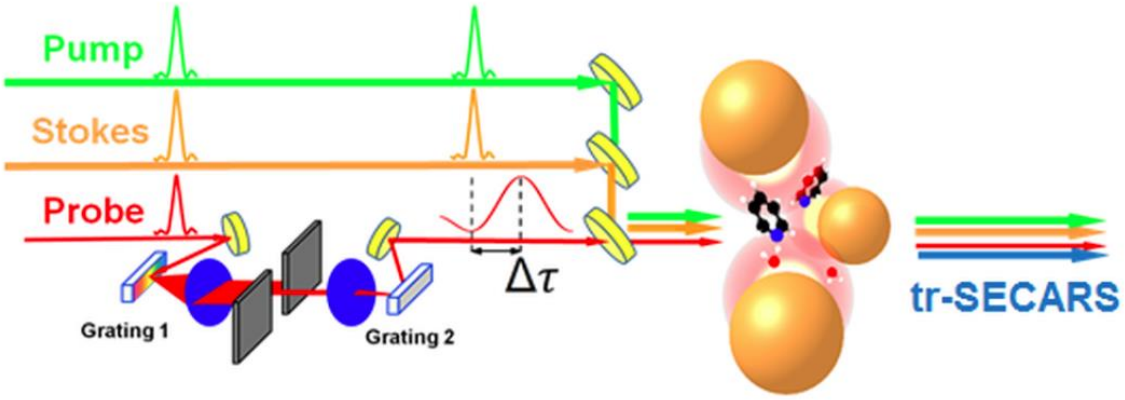

Figure 22 Simplified experimental setup of tr-SECARS spectroscopy. Three laser beams collinearly excite nanomolar amounts of pyridine in the near-field of gold nanoparticles. The pump (green) and Stokes (orange) broadband femtosecond laser pulses excite a molecular vibrational coherence which is probed by a time-delayed shaped narrowband picosecond probe pulse (red). The probe pulse is Sinc-shaped by a pulse shaper slit. The tr-SECARS signal is generated in the forward direction (blue) and collected by a spectrometer with a 0.1 s integration time.

of the three laser beams incident on a sample were chosen to match the plasmon resonance peak of the aggregated gold NPs (Figure 21). The pump and Stokes are femtosecond broadband pulses at 560 and 600 nm, respectively (FWHM, 60 fs). The probe pulse is shaped by a variable slit of a home-built pulse shaper to have a top-hat-like spectrum at 805nm (Figure 22). The probe pulse is thus stretched to a picosecond duration and acquires a temporal Sinc shape. The variable time delay $\Delta\tau$ scans the probe pulse to suppress the nonresonant background by placing the pump and Stokes pulses at the node of the Sinc shape. This optimized tr-SECARS technique combines the advantages of a broadband

coherent vibrational excitation with high resolution narrowband probing and is well suited for microscopic imaging applications.

Typical two-dimensional tr-SECARS spectrograms are shown in Figure 23 – Figure 28 with and without gold nanoparticles for different slit sizes. The signal intensity (log) is plotted as a function of the probe pulse delay $\Delta\tau$ (x-axis) and as a function of the Raman shift (y-axis). The spectrograms were normalized and leveled by subtracting a constant offset. We used low excitation energy (50, 50 and 100 nJ per pulse for the pump, Stokes and probe beams, respectively) to prevent optical damage of gold NPs. Samples of the $12\mu m$ pyridine layer with gold NPs show strong well-resolved signals (Figure 23, Figure 25 and Figure 27). However, no signals were obtained in the absence of NPs under similar conditions (see Figure 32 (green) and discussion below). To compare the signals with and without NPs we increased the thickness of the pyridine layer to 2 mm and obtained signals of similar strength as for the 12 μm layer samples with NPs (Figure 24, Figure 26 and Figure 28). Strong nonresonant background is observed around the zero probe pulse delay time when the pump, Stokes and probe pulses overlap. However, the molecular coherence created by the pump and Stokes pulses decays on a longer time scale than the duration of these pulses. Therefore the pyridine Raman signals are identified even up to 10 ps delay.

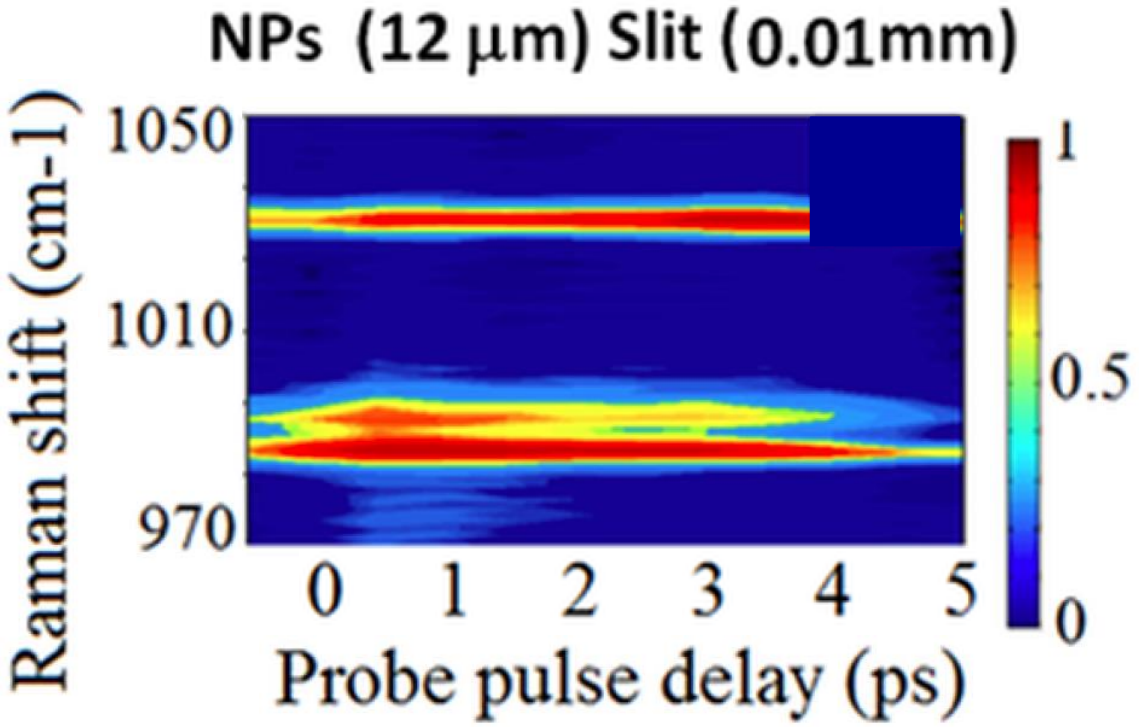

Figure 23 2D spectrogram obtained by scanning the probe pulse delay. Slit size is 0.01 mm. With nanoparticles, the spectrogram resloves three pyridine Raman lines without spectral overlap.

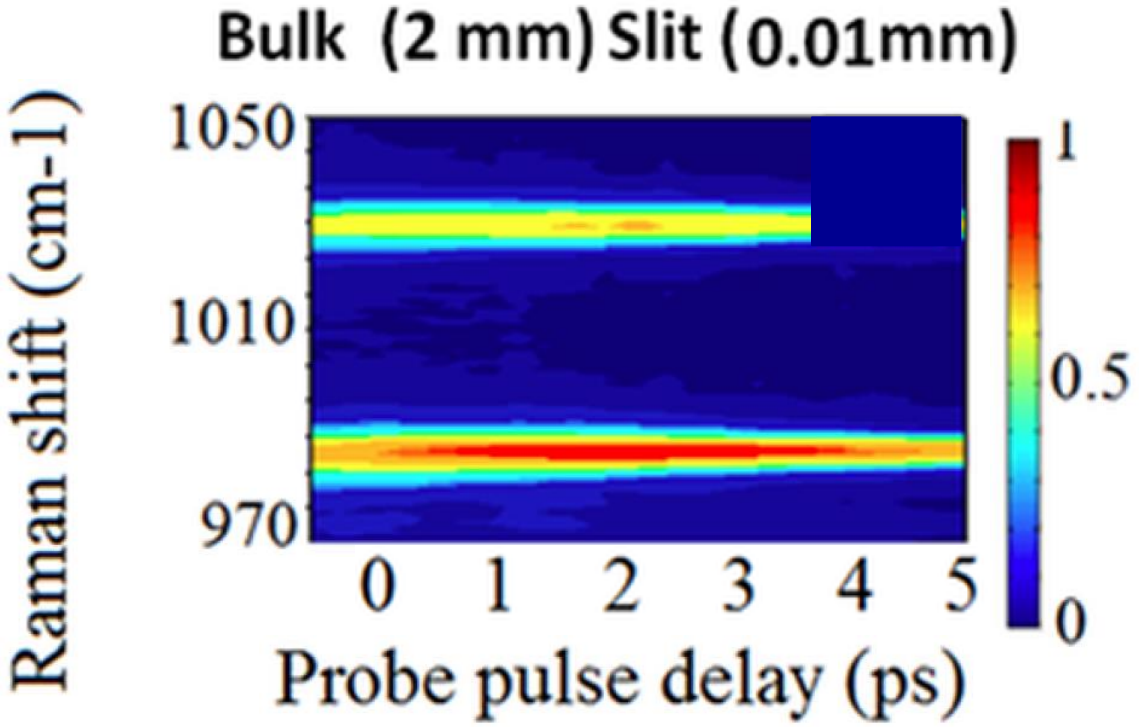

Figure 24 2D spectrogram obtained by scanning the probe pulse delay. Slit size is 0.01 mm. Without nanoparticles, the spectrogram resloves two pyridine Raman lines without spectral overlap.

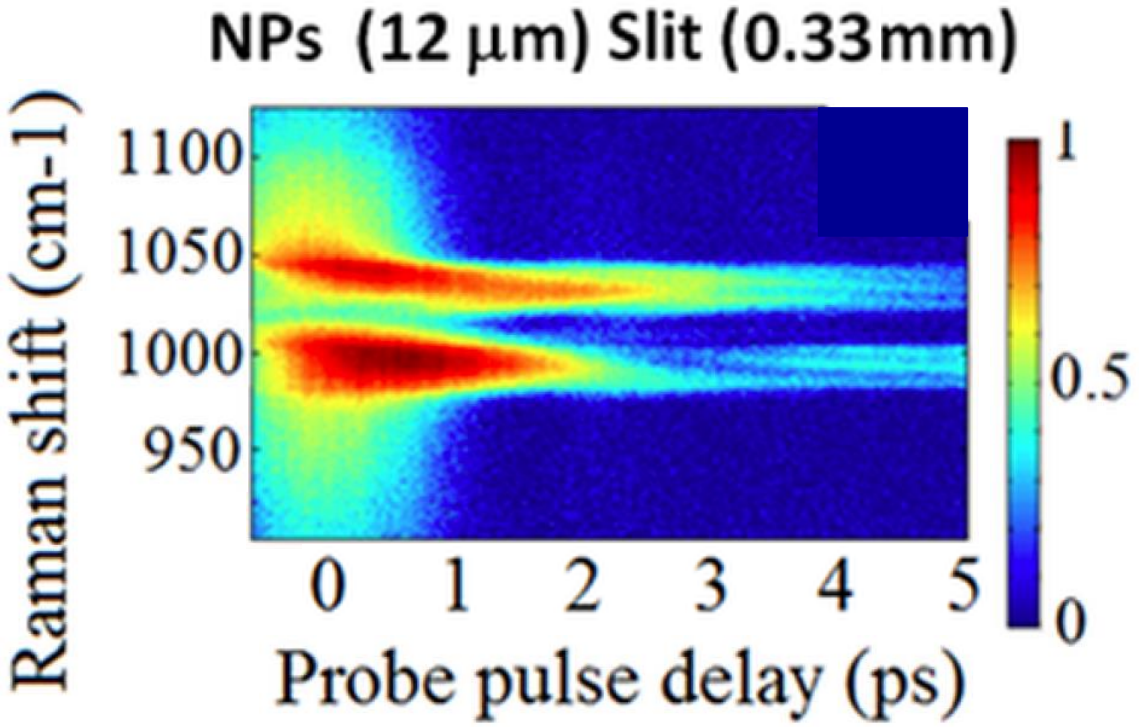

Figure 25 2D spectrogram obtained by scanning the probe pulse delay. Slit size is 0.33 mm. With nanoparticles, the spectrogram resloves three pyridine Raman lines, with two lines at 990 cm^{-1} overlaped.

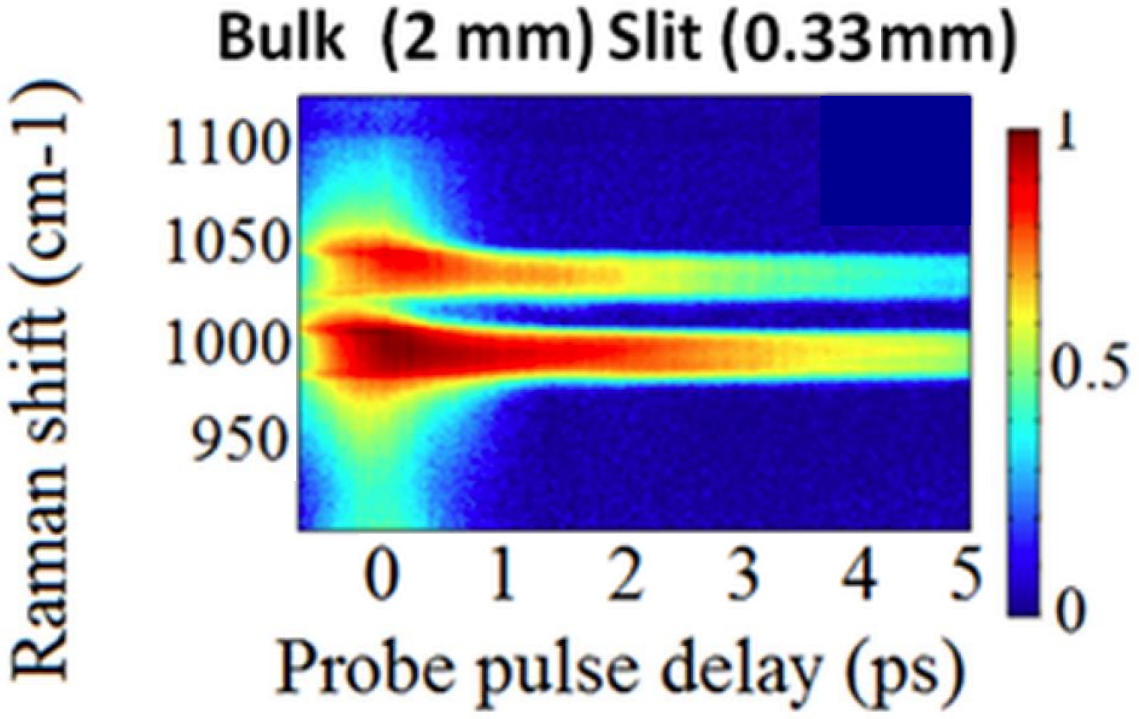

Figure 26 2D spectrogram obtained by scanning the probe pulse delay. Slit size is 0.33 mm. Without nanoparticles, the spectrogram resloves two pyridine Raman lines, without spectral overlap.

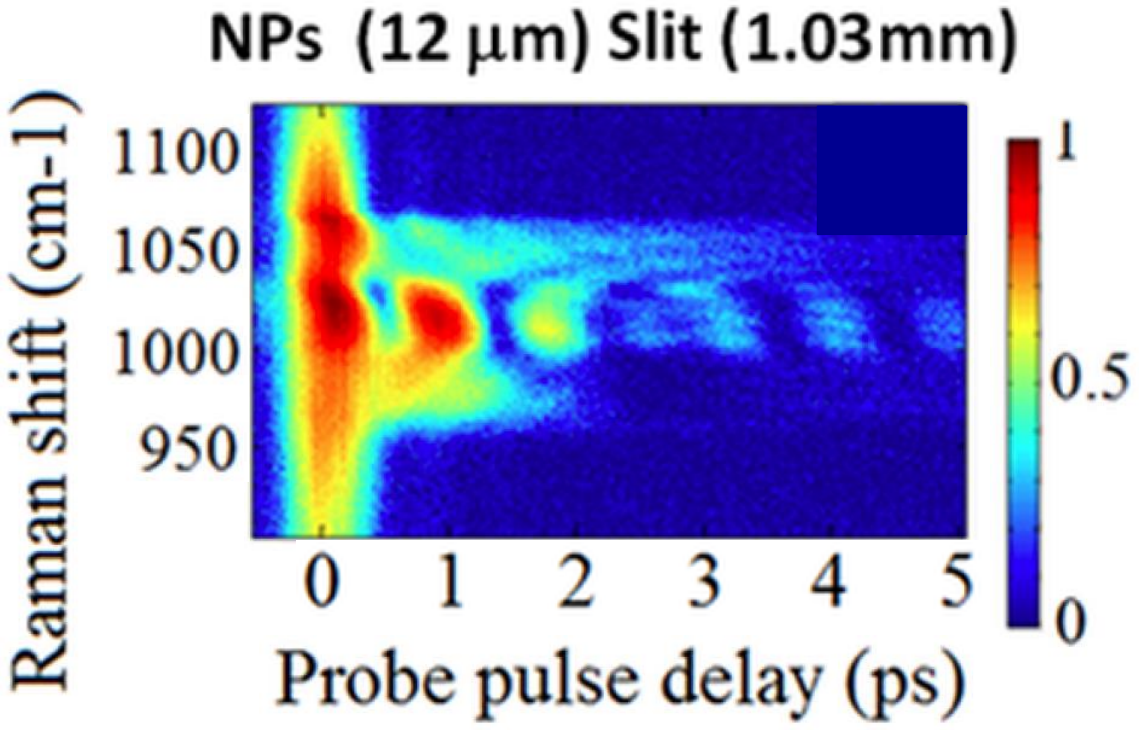

Figure 27 2D spectrogram obtained by scanning the probe pulse delay. Slit size is 1.03 mm. With nanoparticles, the spectrogram resloves three pyridine Raman lines, with complete spectral overlap.

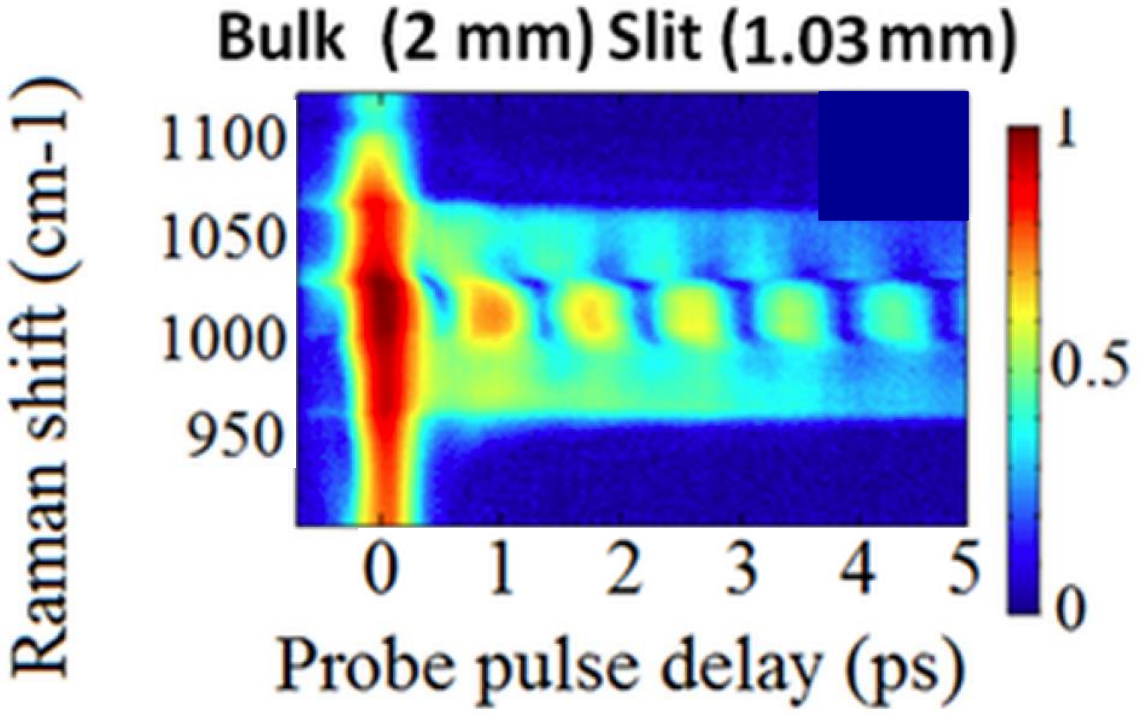

Figure 28 2D spectrogram obtained by scanning the probe pulse delay. Slit size is 1.03 mm. Without nanoparticles, the spectrogram resloves two pyridine Raman lines, with complete spectral overlap.

The spectral resolution is determined by the spectral width of the probe pulse, which, in turn, depends on the slit size. Figure 23 to Figure 28 show tr-SECARS spectrograms for the slit sizes of 0.01, 0.33 and 1.03 mm with qualitatively different Raman spectra and decay dynamics. These slits correspond to the probe pulse width of 5, 22 and 65 cm^{-1}, respectively. The spectrograms for a small slit (0.01 mm) revealed an additional blue-shifted line at ~ 997 cm^{-1} (Figure 23) which was absent in bulk pyridine (Figure 24). The spectra with NPs were sensitive to the position of the laser focal spot on

the sample and showed spatial intensity variations of this signal due to the presence of randomly distributed hot spots. For larger slits, the decreased resolution leads to quantum beating patterns due to spectral overlaps of several resonances. The samples with nanoparticles show more complicated beat patterns due to formation of pyridine complexes (Figure 25 and Figure 27).

III.E. Optimal time delay estimation

We estimate the optimal time delays for background subtraction from the 1D cross-sections (Figure 29) of the 2D SECARS spectrograms (Figure 25 and Figure 26). These plots may be compared with the 1 ps delay plots in Figure 32. The optimal 1 ps delay spectra show stronger signals and lower background.

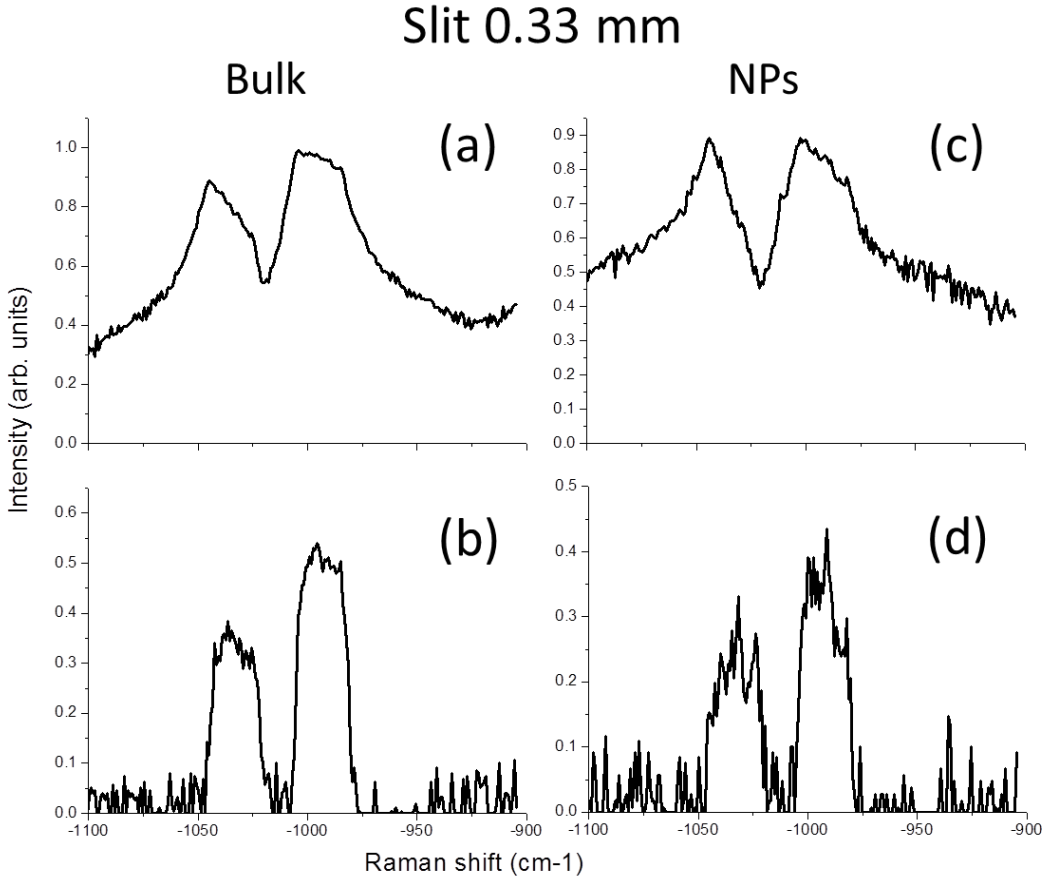

Figure 29 Cross-sections of the 2D tr–SECARS spectrograms for bulk pyridine (a), (b) and pyridine in the near-field of gold NPs (c), (d). The probe pulse delay $\Delta\tau$ is 0 ps in (a), (c) and 5 ps in (b), (d).

III.F. 2D spectrogram analyze

We carried out a detailed analysis of 2D spectrograms (Figure 23 - Figure 28) by taking 1D traces along the x- and y-axes of these 2D spectrograms at the maxima of the Raman signals and for 1 ps probe pulse delay, respectively (Figure 30 – Figure 35).

Figure 30 shows the normalized spectra of pyridine for the 0.01 mm slit with (red) and without (blue) gold NPs. The spectra are shown for the optimal probe delay of 1 ps which corresponds to the largest signal and smallest nonresonant background. A new blue-shifted vibrational mode of pyridine with NPs at ~ 997 cm^{-1} is clearly resolved. However, the nonresonant background is not completely suppressed for this slit size due to the long duration of the probe pulse (several ps). The corresponding temporal traces for each mode are shown in Figure 31. These traces are convolutions of the probe pulse shape and exponential decays of the vibrational coherences. To extract the decay dynamics it is necessary to perform deconvolution analysis and to characterize the probe pulse shape. This can be avoided by decreasing the probe pulse duration using a larger slit width.

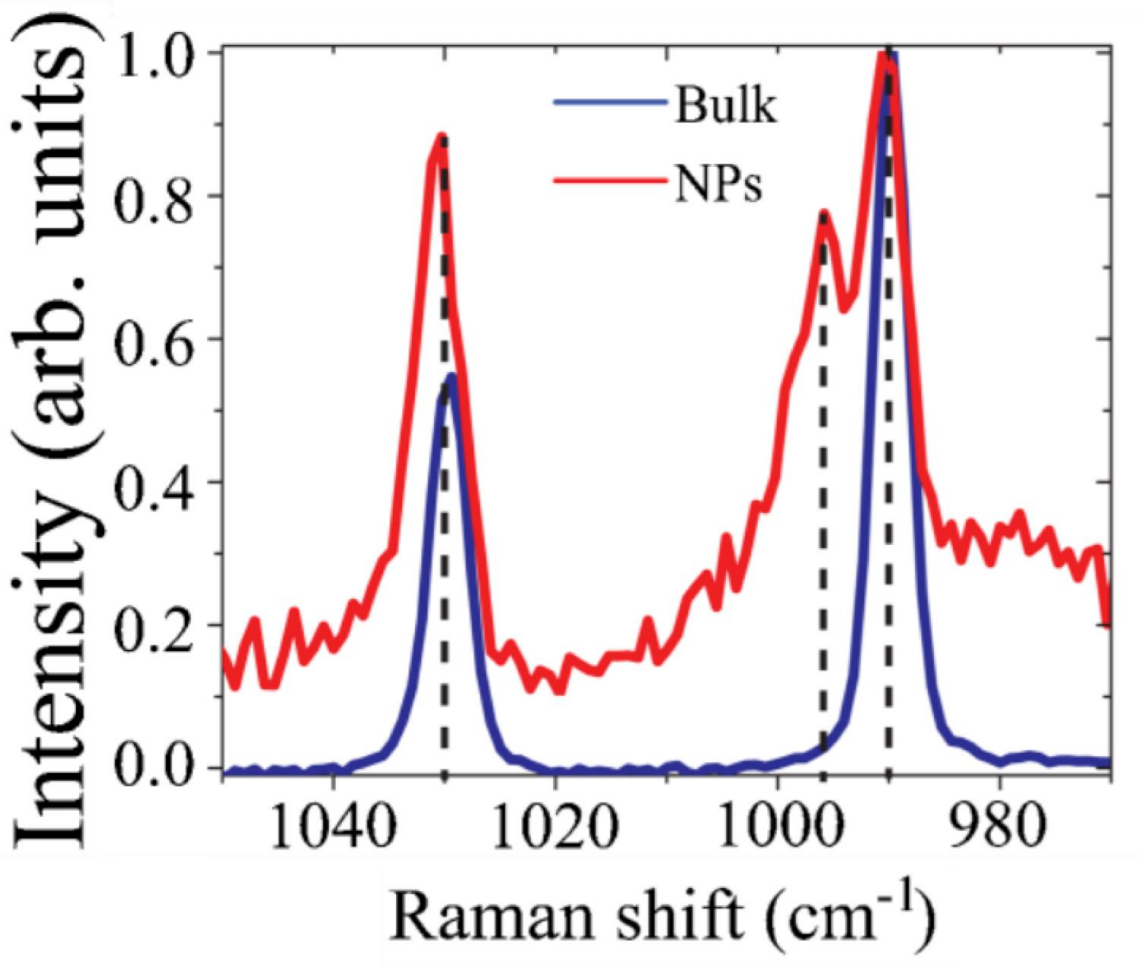

Figure 30 Normailized spectra for 1 ps delay of pyridine with (red) and without (blue) gold nanoparticles (NPs) obtained from the 2D spectrogram of Figure 23 and Figure 24. Signals with NPs wre obtained from 12 μm thick layers of pyridine on the surface of NPs (red). Bulk signals without NPs were obtained under similar excitation conditions from 2 mm thick layers (blue). This spectra corrospond to the 0.01 mm slit and the case of a narrow line width with little spectral overlap. Three modes (dashed) are resolved with NPs (red): at 990 cm^{-1} and 997 cm^{-1} due to the ring breathing mode of free pyridine and hydrogen-bonded pyridine-water complexes, respectively; and at 1030 cm^{-1} due to the triangle mode of a mixture of both species. However, only two modes are observed without NPs (blue):at 990 cm^{-1} and 1030 cm^{-1} indicating no presence of water in the bulk pyridine.

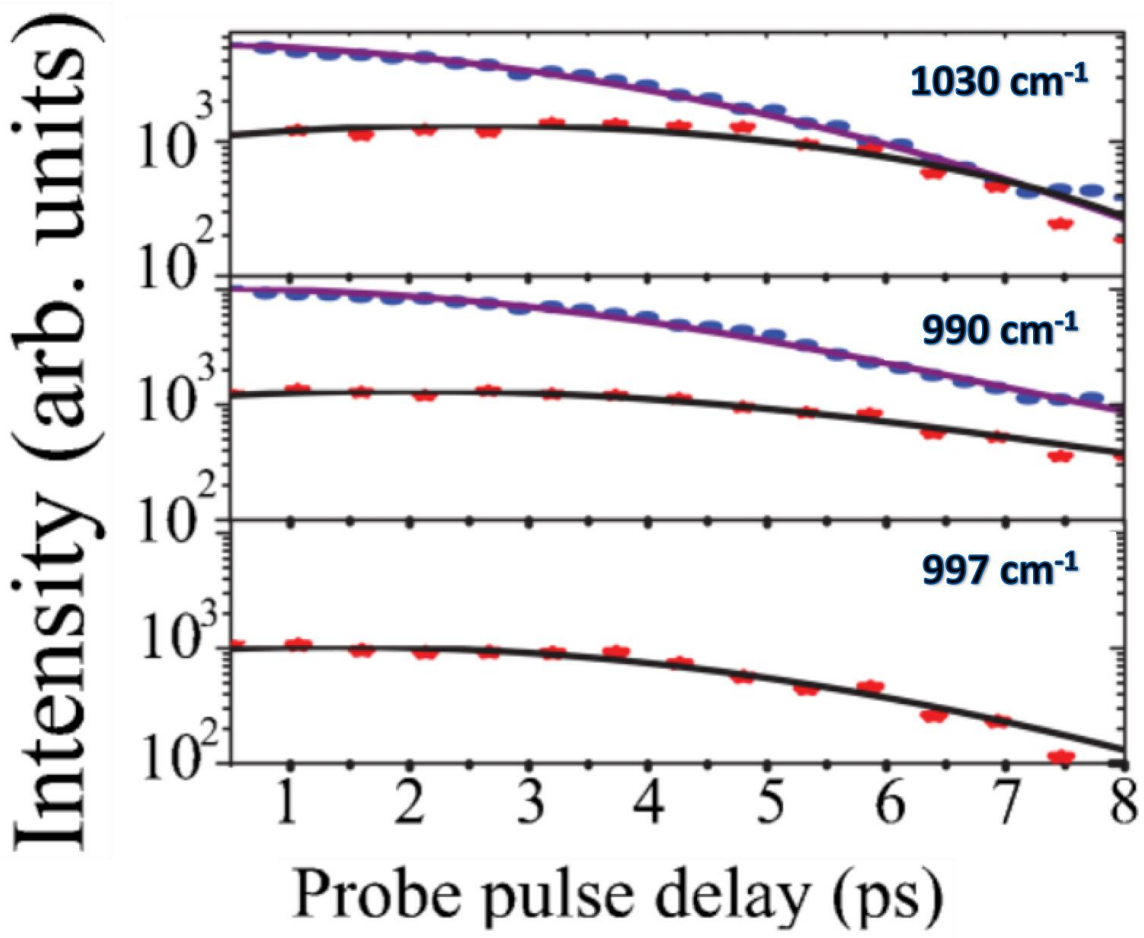

Figure 31 Temporal traces of pyridine with (red) and without (blue) gold nanoparticles (NPs) obtained from the 2D spectrograms of Figure 23 and Figure 24. The temporal traces are convolutions of the vibrational dephasing (1030 cm^{-1}, 990 cm^{-1} and 997 cm^{-1} modes corrosponding to Figure 30, respectively) with shaped probe pulse temporal profiles.

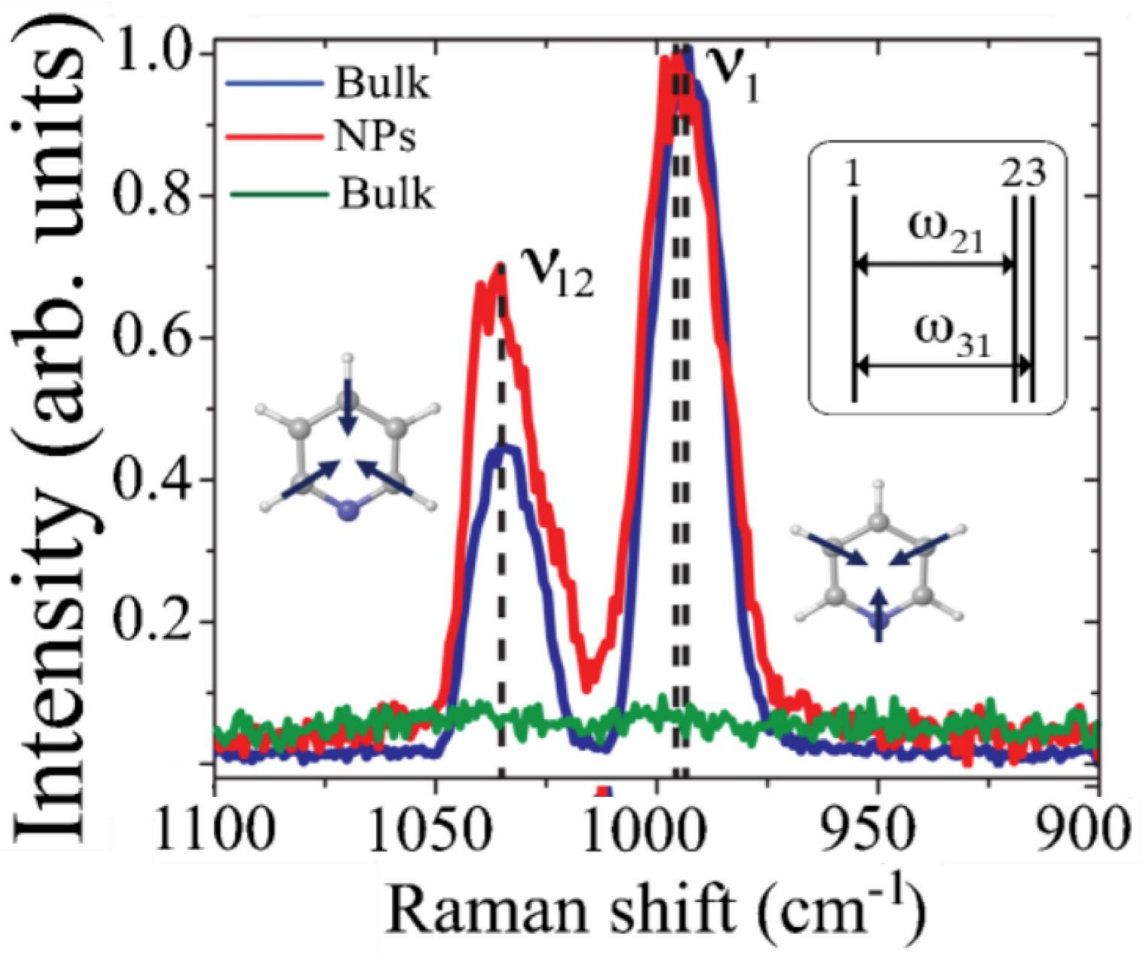

Figure 32 Normalized spectra for 1 ps delay of pyridine with (red) and without (blue, green) gold nanoparticles (NPs) obtained from the 2D spectrograms of Figure 25 and Figure 26. Signals with NPs were obtained from 12 μm thick layers of pyridine on the surface of NPs. Bulk signals without NPs whoed no detectable spectral features for 12 μm thick samples (green). Bulk signals without NPs were obtained under similar excitation conditions from 2 mm thick layers (blue). The spectra correspond to the 0.33 mm slit and intermediate case of partial spectral congestion: two spectral lines are resolved both with (red) and without (blue) NPs. The ring breathing mode of the pyridine-water complex is not resolved.

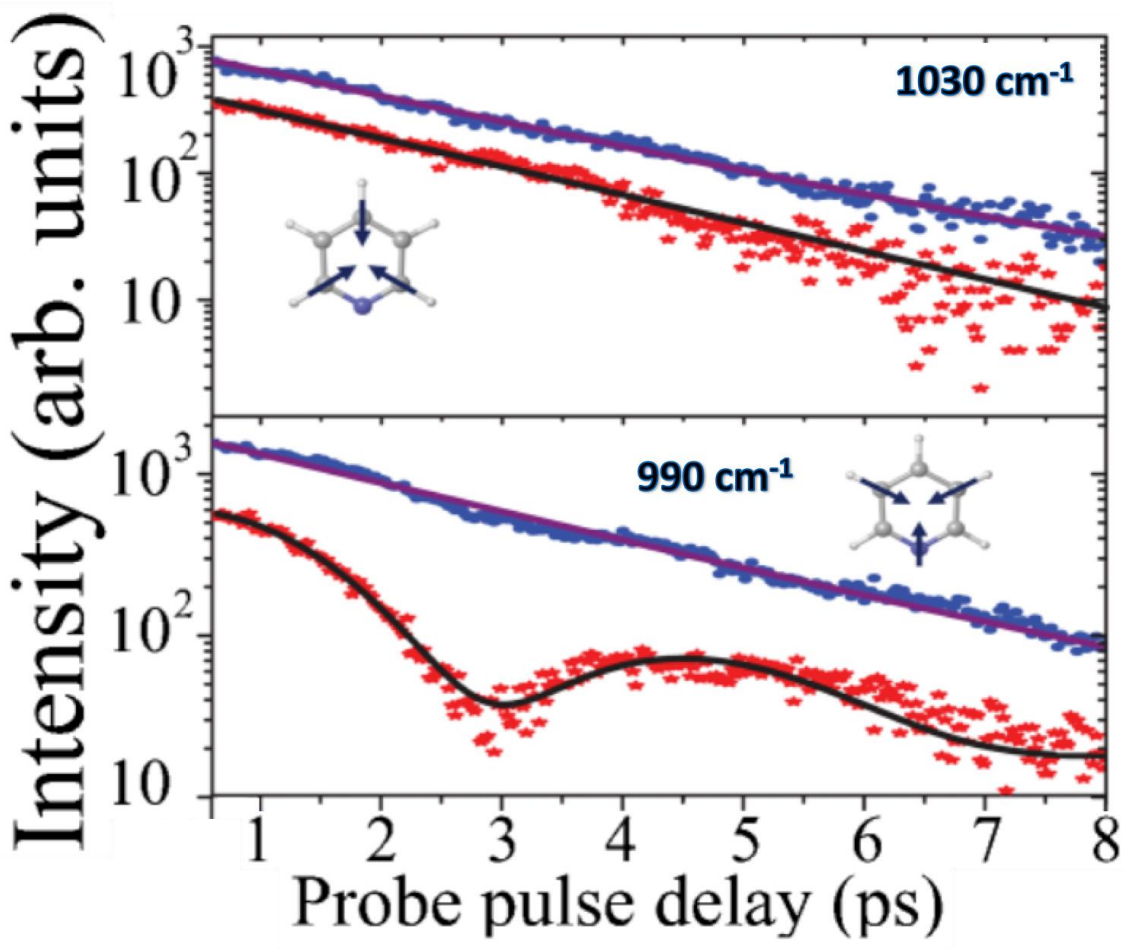

Figure 33 Temporal traces of pyridine with (red) and without (blue) gold nanoparticles (NPs) obtained from the 2D spectrograms of Figure 25 and Figure 26. The temporal traces are corrospongding to 1030 cm^{-1} and 990 cm^{-1} in Figure 32. The ring breathing mode of the pyridine-water complex can be extracted from the temporal trace 990 cm^{-1} mode, where the vibrational dephasing is deconvoluted from the probe pulse shape.

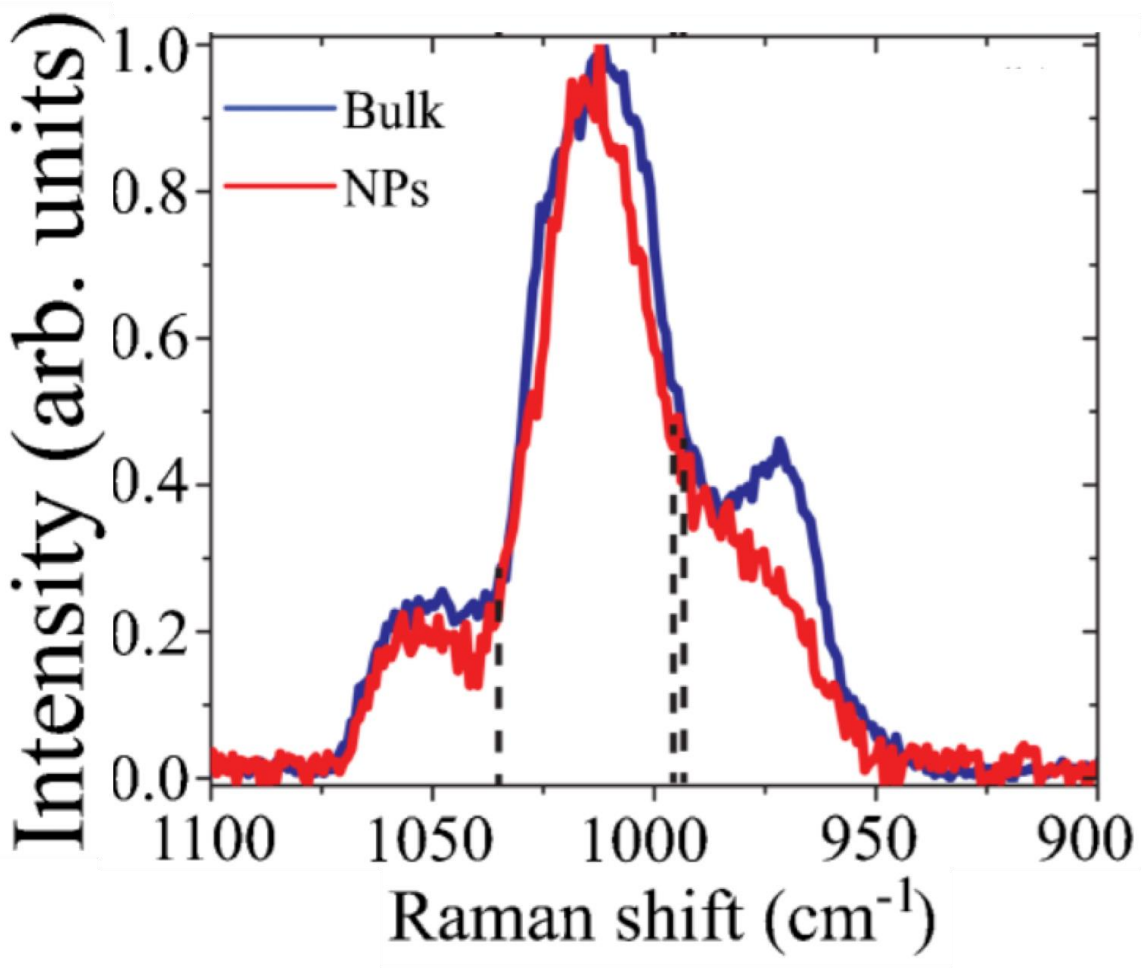

Figure 34 Normailized spectra for 1 ps delay of pyridine with (red) and without (blue) gold nanoparticles (NPs) obtained from the 2D spectrogram of Figure 27 and Figure 28. Signals with NPs wre obtained from 12 μm thick layers of pyridine on the surface of NPs (red). Bulk signals without NPs were obtained under similar excitation conditions from 2 mm thick layers (blue). This spectra corrospond to the 1.03 mm slit where all spectral lines are congested and no modes are spectrally resolved.

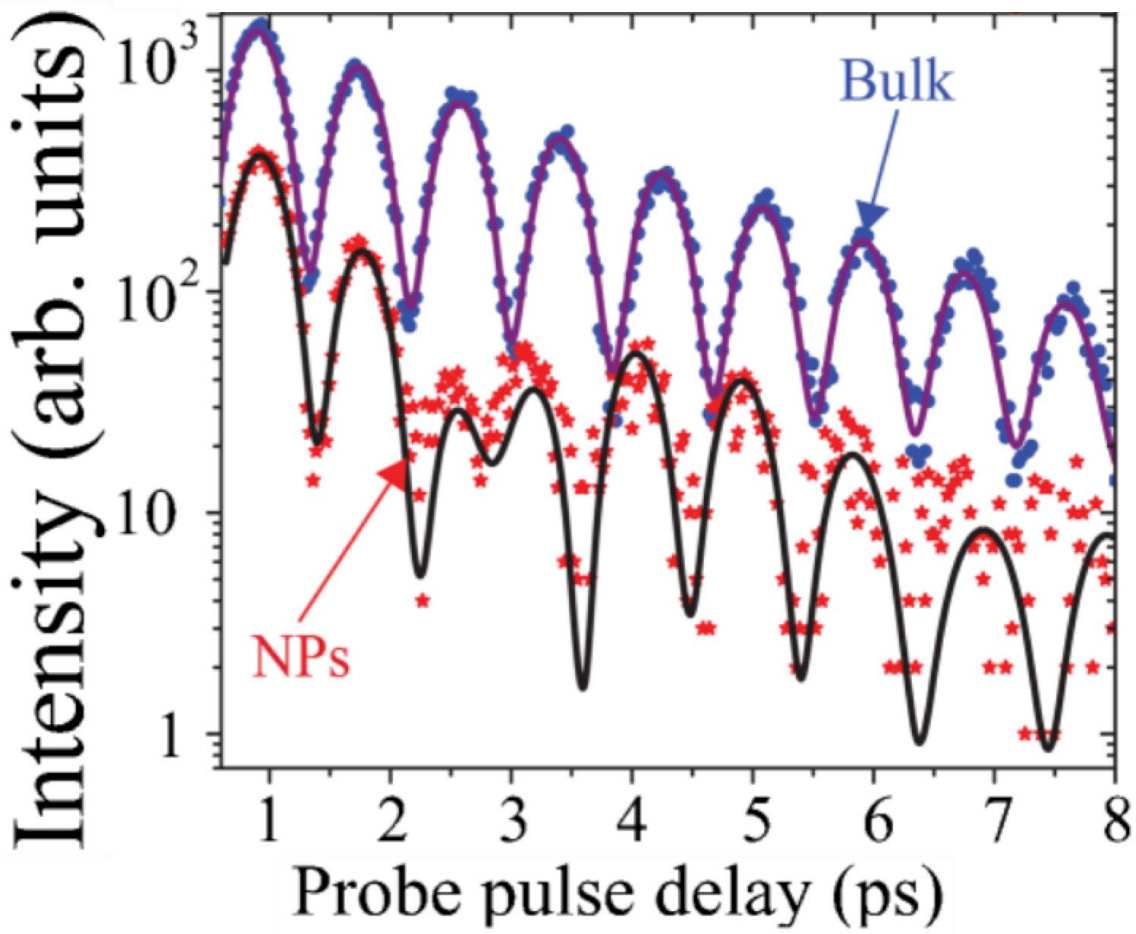

Figure 35 Temporal traces of pyridine with (red) and without (blue) golad nanoparticles (NPs) obtained from the 2D spectrograms of Figure 27 and Figure 28. The time-resolved traces corrospoding to Figure 34 can be used to obtain both dynamical and structural information. However all information is convoluted, and complicated fitting analysis is required. Tr-SECARS provides the advantaed of using both spectral and temproal dimensions simultaneously to extract the relevant structural and dynamical information.

We consider two cases with a larger slit width of 0.33 (Figure 32 and Figure 33) and 1.03 mm (Figure 34 and Figure 35). The spectra in Figure 32 for 1 ps probe delay show two lines both with (red) and without (blue) NPs, which are different only by the amplitude ratios. Therefore, from these spectra alone it is not possible to deduce the existence of the third, blue-shifted transition due to the presence of nanoparticles. However, the temporal traces provide this information via quantum beats (Figure 33). In Figure 33 both traces for the 1030 cm^{-1} triangle mode (with (red) and without (blue) NPs) decay monotonously. However, the 990 cm^{-1} ring breathing mode with NPs (red) in Figure 33 exhibits a pronounced modulation caused by a quantum beating between two resonances. In this case, the probe pulse duration is short enough for the temporal traces to directly reveal vibrational dephasing dynamics, which can be easily analyzed.

Upon a further increase of the slit size the probe pulse duration approaches that of the original unshaped femtosecond pulse and all the spectra become congested (Figure 34). It is not possible to assign modes from any spectrum at one time delay. This drawback can be overcome by performing a time-resolved spectral measurement and analysis of the temporal traces. Figure 35 shows a periodic quantum beating pattern for bulk pyridine without NPs (blue) and a more complicated beating pattern for pyridine with NPs (red). We fit these curves by a sum of three exponential functions and obtain vibrational dephasing, rates which correspond to the previously resolved modes (the fitting procedure and the results are summarized in the next section). Decreasing the slit size yields better spectral resolution but larger nonresonant background due to the longer temporal duration

of the probe pulse. The optimum is found for the 0.33 mm slit which shows narrow spectral lines and small background in Figure 32.

III.G. Temporal traces curve fitting

To fit the experimental data we used a general expression for CARS intensity

$$I_{CARS} = \left| A_1 \exp(-\frac{t}{\tau_1}) + A_2 \exp(-\frac{t}{\tau_2}) \exp[i(\omega_{21}t - \varphi_{21})] + A_3 \exp(-\frac{t}{\tau_3}) \exp[i(\omega_{31}t - \varphi_{31})] \right|^2 \quad (1)$$

Here A_i is the amplitude of peak i with a corresponding lifetime τ_i. We investigated a spectral range of two dominant Raman peaks of pyridine, which correspond to a ring breathing (ν_1) and a triangle (ν_{12}) vibrational mode. Using tr-SECARS we observe a splitting of the ring breathing mode into a doublet. For convenience, we have labeled these peaks 1, 2 and 3 as shown in the inset of Figure 32. The frequencies ω_{21} and ω_{31} correspond to the energy differences between the lines 2 and 3 with respect to 1, respectively. For the data without NPs in Figure 33 (blue circles) at frequency ν_{12} we set $A_2 = A_3 = 0$ and obtained the parameters $A_1 = 32.02 \pm 0.08$ and $\tau_1 = 4.22 \pm 0.06$ ps. In the presence of nanoparticles we obtained $A_1 = 22.89 \pm 0.12$ and $\tau_1 = 3.90 \pm 0.04$ ps (red stars). For Figure 33 without NPs (blue circles) at frequency ν_1, we set $A_1 = A_2 = 0$ and obtained $A_3 = 44.69 \pm 0.12$ and $\tau_3 = 4.80 \pm 0.08$ ps. With NPs (red stars), we set $A_1 = 0$

and obtained $A_2 = 15.48 \pm 1.39$; $\tau_2 = 5.88 \pm 0.06$ ps; $\omega_{21} = 31.44 \pm 2.90$ cm^{-1}; $A_3 = 13.94 \pm 3.08$; $\tau_3 = 2.14 \pm 0.02$ ps and $\omega_{31} = 39.33 \pm 3.03$ cm^{-1}.

For the large slit in Figure 35 without nanoparticles (blue circles), we fixed the parameters $A_2 = 0$; $\tau_1 = 4.22$ ps; $\tau_3 = 4.80$ ps and obtained the parameters $A_1 = 30.57 \pm 0.26$; $A_3 = 17.29 \pm 0.24$; $\omega_{31} = 39.89 \pm 0.04$ cm^{-1}. With nanoparticles (red stars), we fixed $\tau_1 = 3.90$ ps; $\tau_2 = 5.88$ ps; $\tau_3 = 2.14$ ps and obtained $A_1 = 8.87 \pm 0.21$; $A_2 = 5.74 \pm 0.19$; $A_3 = 14.01 \pm 0.36$, $\omega_{21} = 33.79 \pm 0.18$ cm^{-1}; and $\omega_{31} = 41.91 \pm 0.16$ cm^{-1}. The fitting parameters are summarized in Table 1. From the fitting we obtained the ν_1 doublet splitting $\omega_{32} = 8.12 \pm 0.34$ cm^{-1}. We used the same parameter values and convoluted the exponential decays with the Gaussian pulse shapes to fit the curves in Figure 31.

	Fig. 33 ν_{12}		Fig. 33 ν_1		Fig. 35	
Parameters	Bulk	NPs	Bulk	NPs	Bulk	NPs
τ_1 [ps] (A_1)	4.22 (1.00)	3.90 (1.00)	--	--	*4.22* (1.00)	*3.90* (0.63)
τ_2 [ps] (A_2)	--	--	--	5.88 (1.00)	--	*5.88* (0.41)
τ_3 [ps] (A_3)	--	--	4.80 (1.00)	2.14 (0.90)	*4.80* (0.57)	*2.14* (1.00)
ω_{21} [cm^{-1}]	--	--	--	31.44	--	33.79
ω_{31} [cm^{-1}]	--	--	--	39.33	39.89	41.91

Table 1 Fitting parameters for the temporal profiles of Fig. 32 -35. The amplitudes A_i in each fit are normalized to a line with a highest intensity.

III.H. Enhancement

Among many approaches to estimate the enhancement factor (EF) [5, 10, 14], we used direct scaling of spectral amplitudes. We estimate the enhancement factors (EF) based on a direct comparison of the signals with and without nanoparticles. CARS signal intensity can be expressed as [64]

$$I_{CARS} \sim I_{pump} I_{Stokes} I_{probe} L^2 \mathrm{sinc}^2 \left[\frac{\Delta kL}{2} \right]. \quad (2)$$

For perfect phase matching, we estimate EF by comparing the tr-SECARS signals obtained from a 12 μm thick layer of pyridine on random aggregated gold NPs (SignalNPs) and a 2 mm cell of pure pyridine without NPs (Signalno NPs) for selected spectral peaks as

$$EF = \frac{Signal_{NPs} / L_{NPs}^2}{Signal_{no\ NPs} / L_{no\ NPs}^2}. \quad (3)$$

We take the slit width 0.33 mm data set as an example. As described above, the signals with (red) and without (blue) NPs are obtained for the 12 μm and 2 mm layers of pyridine, respectively. Spectra of the 12 μm layers without NPs (Bulk, green) show no detectable signals (Figure 32). Therefore, in order to estimate the surface enhancement factor we compare signals for the 12 μm (NPs) and 2 mm (bulk) layers. We assume that the signals with gold NPs are generated from ~ 50 nm layers of pyridine which corresponds to an upper bound extension of NP near fields (Figure 16). Taking into account the finite coherence length in the sample and the focusing length of laser beams

we estimate that the signals without NPs are generated from, 300 μm layer of bulk pyridine. Normalizing the ratios of the signals in Figure 32 yields the enhancement factor of ~ 10^7. It is six orders of magnitude more than previously reported using femtosecond SECARS from a silver colloid [51], and two orders of magnitude higher than from a structured surface [52]. Also, compared to femtosecond SECARS in ref. [52], it has a higher spectral resolution and lower nonresonant background. This value is closer to the theoretical estimate of ~ 10^{10} for isolated NPs [65].

III.I. Quantum chemistry calculations

Using tr-SECARS we obtained both spectral and temporal information from nanoscale volumes of pyridine in the vicinity of gold NPs. The spectra enable the characterization of the nature of pyridine complexes with other molecular species on the surface and the dynamics reveal their function. Using density functional theory (DFT) we calculated the equilibrium structures and Raman frequency shifts of various complexes of pyridine, water, and gold clusters. The calculated vibrational wave numbers of pyridine ring breathing (B) and triangle (T) modes are listed in Table 2 - Table 3. Our simulation results show that in different complexes the triangle mode is within ~ 3 cm^{-1} of the bulk pyridine (Figure 20). In contrast, the ring breathing mode shows a significant variation of shifts towards higher values. The shift due to pyridine-water hydrogen bond formation is smaller than the shift caused by the pyridine-gold interaction and matches well with the experimentally determined value of ~ 7 cm^{-1}. (The overall blue shift of the simulated

signals with respect of the experimental value is due to quantum chemical approximations.) Therefore we conclude that the pyridine-water complex provides the most significant contribution to the observed tr-SECARS spectra (number 1 in Figure 15 and Figure 20). Thus, tr-SECARS allows the detection of a small amount of water on the surface of gold nanoparticles. Previous studies reported similar line shifts observed from bulk mixtures of pyridine and water at silver surfaces [6]. In contrast, here we considered pure pyridine. Water is found as a small impurity on the surface of gold, which may have been adsorbed from the ambient air.

Pyridine	Mode	Freq	
		Harmonic	Anharmonic
Experiment	B		990
	T		1030
B3LYP/6-31G*	B	1012	997
	T	1051	1035
B3LYP/cc-pVDZ	B	1009	994
	T	1048	1032
B3LYP/cc-pVTZ	B	1012	998
	T	1052	1036
B3LYP/aug-cc-pVDZ	B	1007	992
	T	1045	1029
B3LYP/aug-cc-pVTZ	B	1012	996
	T	1051	1033
MP2/6-31G*	B	1015	1002
	T	1057	1042
MP2/cc-pVDZ	B	1006	992
	T	1045	1029

Table 2 Harmonic and anharmonic vibrational frequencies (cm^{-1}) for pyridine modes: ring breathing (B) and triangle (T) modes as obtained from calculation using various levels of theory.

System	Mode	Expt.	B3LYP/CC-PVDZ	
			Harmonic	Anharmonic
Pyridine	B	990	1009	994
	T	1030	1048	1032
Pyridine-Water	B	1000	1018	1002
	T	1033	1047	1030
Pyridine-$(Water)_2$	B		1024	1007
	T		1047	1031
$(Pyridine)_2$-Water	B		1016	998
	T		1046	1030
Pyridine-Gold	B		1022	1005
	T		1045	1029
Pyridine-$(Gold)_2$	B		1033	1018
	T		1048	1033
Pyridine-$(Gold)_8$	B		1028	1015
	T		1048	1032
Pyridine-$(Water)_2$-Gold	B		1030	-
	T		1048	-

Table 3 Harmonic and anharmonic vibrational frequencies (cm^{-1}) for pyridine modes: ring breathing (B) and triangle (T) modes as obtained from B3LYP/CC-PVDZ level of calculations.

III.J. Discussion

Here we report a first observation of nanoscale pyridine-water complexes using time-resolved surface-enhanced coherent Raman (tr-SECARS) spectroscopy. These complexes were not observed in the SERS spectra. This result highlights the differences between SERS and tr-SECARS. Different laser frequencies, powers, and acquisition times do not allow a direct comparison of the enhancement factors. We used a high power cw

Nd:YAG laser to obtain the SERS signals in a reasonable time of ~ 80 s. This continuous perturbation might have caused degradation of the hydrogen-bonded complexes. On the other hand, tr-SECARS uses ultrashort laser pulses at 1 kHz repetition rate with the total sub-nanosecond perturbation time of the system. This may have particular advantages for the investigation of fragile molecular complexes in biological systems, which cannot sustain high-power SERS laser sources. Investigation of such biocomplexes at nanoscale requires depositing even more laser power to obtain good signals. Tr-SECARS provides a promising alternative route towards this goal. This method presents new promising opportunities for high resolution and high sensitivity characterization of nanoparticle surfaces and nanoscale biomolecular complexes.

Tr-SECARS spectroscopy could be used to detect small amounts of toxic substances such as anthrax due to higher sensitivity compared with conventional coherent Raman techniques. Optimal pulse shapes could be found using open-[66] and closed-loop[67] coherent control methods applied on the nanoscale. Improvements of sample preparation could also increase enhancement factors. Resonant optical nanoantennas[68] could be designed for optimal tr-SECARS signals controlled by pulse shaping[69]. Time-resolved tip-enhanced CARS spectroscopy[49] and subwavelength microscopy could be realized by extension of the present approach. Spectral interpretation could be facilitated by using higher levels of theory and by direct modeling of the surface-enhanced CARS signals[70]. With further developments tr-SECARS could achieve ultrashort sub-picosecond signal acquisition and single shot real-time detection capabilities. Other related surface-enhanced nonlinear optical spectroscopic techniques could be developed

based on the present approach[71]. Various coherent multidimensional optical spectroscopies could be implemented on the nanoscale that would benefit from the improved spectral and spatial resolution and higher sensitivity [72, 73]. It would be possible to directly probe subwavelength vibrational and electronic response functions of complex artificial and biological systems in real time. Finally, tr-SECARS could be used as a new method for studying coherent dynamics of nanowater on the surface of biomolecules or in confined nanowires [74] for biomedical and nanofluidic applications.

CHAPTER IV

NATURE OF SURFACE-ENHANCED COHERENT RAMAN SCATTERING*

Surface-enhanced coherent nonlinear optical signals could dramatically improve detection sensitivity of spectroscopic imaging techniques. Large enhancement factors (EFs) of many orders of magnitude are expected for coherent Raman scattering of molecules in local fields of plasmonic nanostructures. However, only small EFs, several orders of magnitude less than the predicted values, were experimentally observed. To understand this discrepancy we measured the spatial variation of the shape of surface-enhanced coherent anti-Stokes Raman scattering (SECARS) spectra of pyridazine on randomly aggregated gold nanoparticles. We developed a model to simulate the dependence of SECARS spectra on the position and linewidth of the surface plasmon resonance, and attribute small (and even negative) EFs to local destructive interference. We report measurements of nanoscale phase effects in SECARS, and propose strategies to increase experimental EFs towards theoretical predictions.

*Reprinted with permission from "Nature of surface-enhanced coherent Raman scattering" by Xia Hua, Dmitri V. Voronine, Charles W. Ballmann, Alexander M. Sinyukov, Alexei V. Sokolov, and Marlan O. Scully, 2014. *Physical Review A,* vol. 89, pp. 043841, Copyright [2014] by American Physical Society.

IV.A. Introduction

Coherent nonlinear optical spectroscopy provides rich information about the structure and dynamics of atoms and molecules [73]. Various techniques such as second-harmonic generation (SHG), third-harmonic generation (THG), sum and difference-frequency mixing, four-wave mixing (FWM), coherent Raman scattering, and others, in a wide range of frequencies from microwaves to x rays, probe rotational, vibrational, and electronic motion. Coherent Raman scattering microscopy, in particular, provides chemical maps of live cells and tissues, and has been used in biomedical applications [75-77]. Extension of these techniques to the nanoscale is challenging. Various strategies have been used to suppress the nonresonant background of coherent Raman signals based, for example, on polarization [78], phase effects [79-81], frequency modulation [82], time delay [83], and laser pulse shaping [53, 59, 84-86]. New nano-optical methods have been developed to enhance weak signals and to obtain nanoscale resolution [87]. Surface enhancement of linear optical signals due to strong local fields of plasmonic nanostructures has been successfully used in fluorescence, absorption, and spontaneous Raman scattering experiments [5, 10, 11, 88]. However, surface-enhanced coherent nonlinear optical signals have been less explored. For example, proof-of-principle demonstrations of surface enhanced SHG and THG [89-91], FWM [53, 71, 92, 93], and coherent anti-Stokes Raman scattering (SECARS) [13, 47-52, 65, 94-96] have been reported, but the expected large enhancement factors (EFs) were not observed.

Surface plasmon resonances (SPRs) of metallic nanostructures can lead to a strong local field enhancement. The amplitude, position, and linewidth of SPRs depend on the size and shape of nanostructures, and may be tuned by varying structural parameters. Nanostructures can have responses with complex amplitude and phase profiles due to several overlapping resonances. The realistic nanostructures can be synthesized by self-assembly or fabricated using nanolithography. Both methods have certain advantages and limitations, and produce nanostructures with imperfections that result in distributions of SPR properties. For example, randomly aggregated gold or silver nanoparticles can be self-assembled to form fractal-like clusters with a distribution of localized spatial regions of enhanced electric fields, called "hot spots" [97]. Near-field EFs in hot spots reach $\sim 10^1 - 10^3$. Molecules placed in such fields may generate optical signals enhanced by many orders of magnitude. Incoherent spontaneous Raman scattering signal intensity (I_{Raman}) is proportional to the number of molecules (N) and to the intensity of the incident field (I_{in}): $I_{Raman} \sim NI_{in}$. SPRs can enhance both the incident (E_{in}) and the scattered (E_{Raman}) fields by $\sim 10^1 - 10^3$, resulting in $\sim 10^4 - 10^{12}$ enhancement factors $EF_{Raman} \sim |E_{in}|^2 |E_{Raman}|^2$. Such strong surface-enhanced Raman scattering (SERS) signals with EFs close to the theoretical values have been observed [5, 10-12].

Coherent nonlinear optical signals have a higher order dependence on incident electric fields, and can, therefore, have larger enhancement factors than linear signals. For example, the intensity of coherent anti-Stokes Raman scattering (CARS) signals I_{CARS} is proportional to the squared number of molecules and to the intensities of three incident

fields, pump (E_{pu}), Stokes (E_{St}), and probe (E_{pr}): $I_{CARS} \sim N^2 \left|E_{pu}\right|^2 \left|E_{St}\right|^2 \left|E_{pr}\right|^2$. Therefore, one can expect $\sim 10^8 - 10^{24}$ enhancement factors from local fields of plasmonic nanostructures: $EF_{CARS} \sim \left|E_{pu}\right|^2 \left|E_{St}\right|^2 \left|E_{pr}\right|^2 \left|E_{CARS}\right|^2$ (compared to the conventional CARS). An additional chemical enhancement of $\sim 10^2$ has been predicted [70]. These surface-enhanced CARS (SECARS) signals could be used to extend nonlinear Raman microscopy to the nanoscale resulting in many applications. However, until now, several orders of magnitude smaller EFs than those expected for SECARS have been observed, and the reason for this remained unclear. Maximum enhancement of SECARS over conventional CARS signals of $\sim 10^{12}$ was predicted for silver nanospheres [65], but only $\sim 10^1 - 10^3$ was observed [48, 50, 51, 98]. Other substrates were also explored such as randomly aggregated nanoparticles [47, 96] and structured nanovoid substrates, including Klarite [52]. These substrates yielded EFs $\sim 10^5 - 10^7$, which were also smaller than expected, and the measured spectra had large nonresonant background contributions. The SECARS EFs over SERS are expected to be on the same order of magnitude as SERS EFs over spontaneous Raman signals. However, in [52] these were ~ 4 orders of magnitude lower. These discrepancies between the predictions and observations may be resolved by considering the SPR properties such as the local phase and resonant enhancement of surface-enhanced coherent Raman signals.

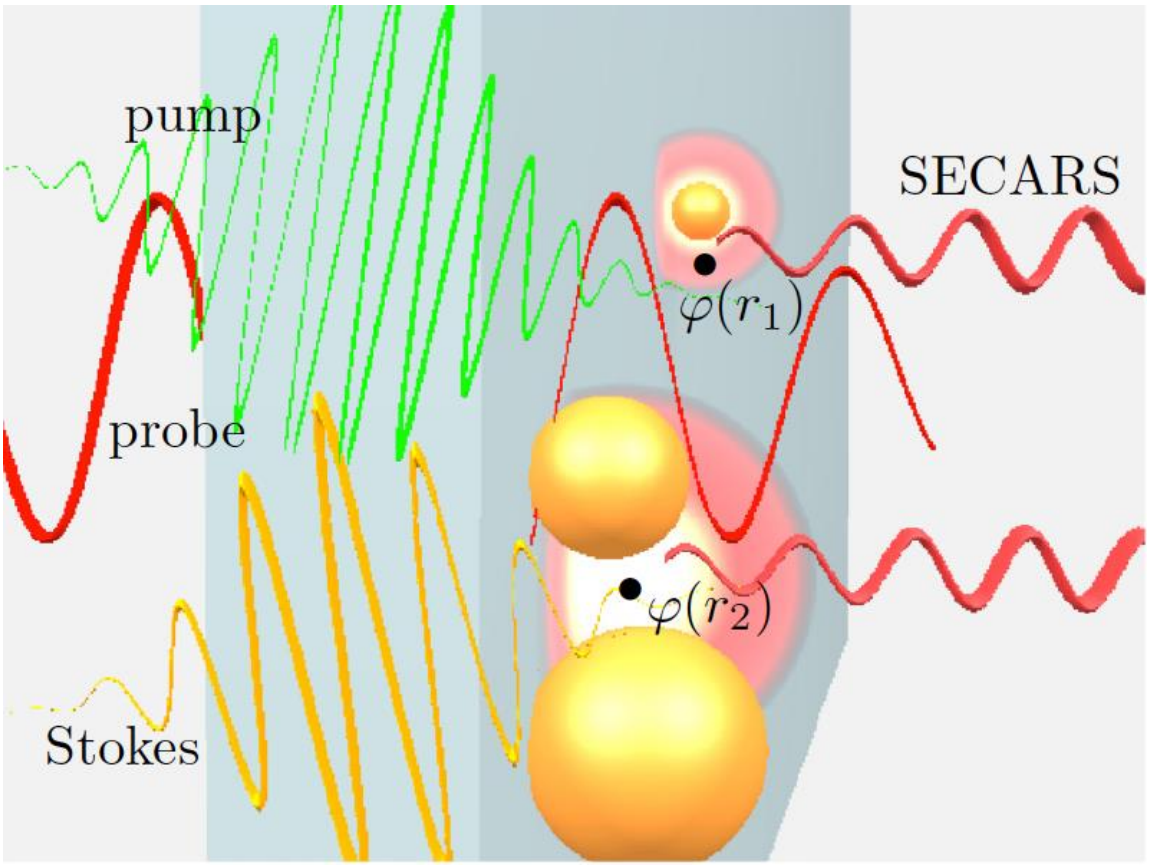

Figure 36 Schematic picture of the surface-enhanced coherent Raman scattering process. Three ultrashort laser pulses are focused on the sample of randomly aggregated gold nanoparticles on the surface of glass inducing SECARS signals from pyridazine molecules in hot spots of the nanoparticles. Different hot spots have different local phase, which lead to different shapes of the SECARS spectra. Averaging over several spots leads to destructive interference and decrease enhancement factors.

Here we investigate these effects by measuring the spatial dependence of the shape of SECARS spectra of pyridazine molecules on the surface of randomly aggregated gold nanoparticles (Figure 36). We also simulate the dependence of the shape of the SECARS

spectra on the SPR position and line-width and use a simple model to explain the results of the measurements. We obtain insights into the nature of surface-enhanced coherent Raman scattering, which allow improving nanostructure design and experimental conditions. These improvements may lead to further signal enhancement resulting in applications in nanoscale bioimaging and ultrasensitive detection.

IV.B. Experimental results

SECARS experiments were performed using the experimental setup described earlier [96]. Briefly, femtosecond pump and Stokes (FWHM ~ 60 fs) and picosecond probe (FWHM ~ 1–2 ps) laser pulses were centered at 560, 600, and 805 nm, respectively (Figure 21), and were generated using an amplified femtosecond Ti:sapphire laser system (Coherent, Inc.) with two optical parametric amplifiers with 1 kHz repetition rate. The probe pulse was shaped by a variable slit of a home-built pulse shaper to have a top-hat-like spectrum. The probe pulse was thus stretched to a picosecond duration and acquired a temporal sinc shape. The pulses were collinearly focused using a 10 cm focal length lens onto the sample of liquid pyridazine sandwiched between two glass slides. Random gold nanoparticle (NP) aggregates were deposited onto the surface of the first glass slide along the laser beam propagation direction. The diameter of the individual gold NPs was 10–20 nm. They formed aggregates upon deposition on glass with surface roughness of 10–300 nm measured by atomic force microscopy (MultiView 4000, Nanonics Ltd.). This surface roughness is necessary for surface plasmon excitation to support a large range of

frequencies. The randomly aggregated NPs formed a nonuniform thin film whose overall thickness can be controlled by varying the concentration of gold NPs in solution. Even though the roughness can be on the order of 300 nm, it strongly depends on the position on the sample. These surface irregularities result in hot spots with strong field confinement and enhancement and with a broad SPR frequency range (500–850 nm) revealed in the absorbance spectrum (Figure 21). The center frequencies of the CARS excitation laser pulses were chosen to fit the SPRs.

The sample preparation procedure was previously described [96]. We used a modified procedure that was previously reported to produce randomly aggregated gold NPs on glass substrates [47, 57]. The synthesis was performed by reduction of $HAuCl_4$ with sodium citrate [47, 57, 58]: 100 ml of 0.1 mM aqueous solution of $HAuCl_4$ was stirred and heated until boiling. Then 10 ml of 0.4 mM aqueous solution of trisodium citrate was added. As a result, individual spherical gold NPs 10–20 nm in diameter were obtained. Microscope slides were cleaned using concentrated sulfuric acid (98%) overnight, trichloroethylene (30 min), acetone (30 min), and methanol (30 min). All the steps were performed at room temperature. Distilled water was used to rinse the substrates. The glass slides were derivatized with 3-mercaptopropyltrimethoxysilane (MPTMS). Clean glass slides were kept in a 5% MPTMS solution in methanol for 24 h [57]. After derivatization, the slides were cleaned with methanol and rinsed with distilled water. Then the gold NPs were deposited onto the glass surface. After $\sim$ 2 h, a layer of aggregated gold NPs was formed.

The excitation laser focal spots of ~ 10 μm diameter were centered on the thin layer of gold NP aggregates extending over a region including glass, gold, and pyridazine (Figure 36). Resonantly excited gold NP aggregates generate many hot spots within the focal region [97], leading to various sources of CARS and nonresonant background. Glass, gold, and pyridazine generate the nonresonant FWM background. Glass occupies the largest volume within the focal spot and therefore we assume glass to be the primary source of the background. This background from glass can be suppressed by stronger focusing of the incident beams on the gold NPs. Then the background from the NPs will dominate [53, 99]. CARS signals originate from bulk pyridazine or from pyridazine in the near field of the gold NPs. We assume that CARS signals originate mostly from the near field of the gold NPs due to the absence of the bulk signal without NPs [96]. We used 12-μm-thick pyridazine samples with gold NPs to perform these measurements. However, no signals were obtained in the absence of NPs under similar conditions. Additional evidence for these assumptions is provided by the results of the present experiments in the spatial dependence of the shape of CARS spectra. No spatial dependence of the CARS shape is expected for bulk samples. The phase of the background is determined by the three incident laser pulses interacting with glass, but the phase of the SECARS signal is determined by the local near fields induced by the gold NP aggregates. The relative phase difference between the background and the local fields determines the shape of the SECARS spectra.

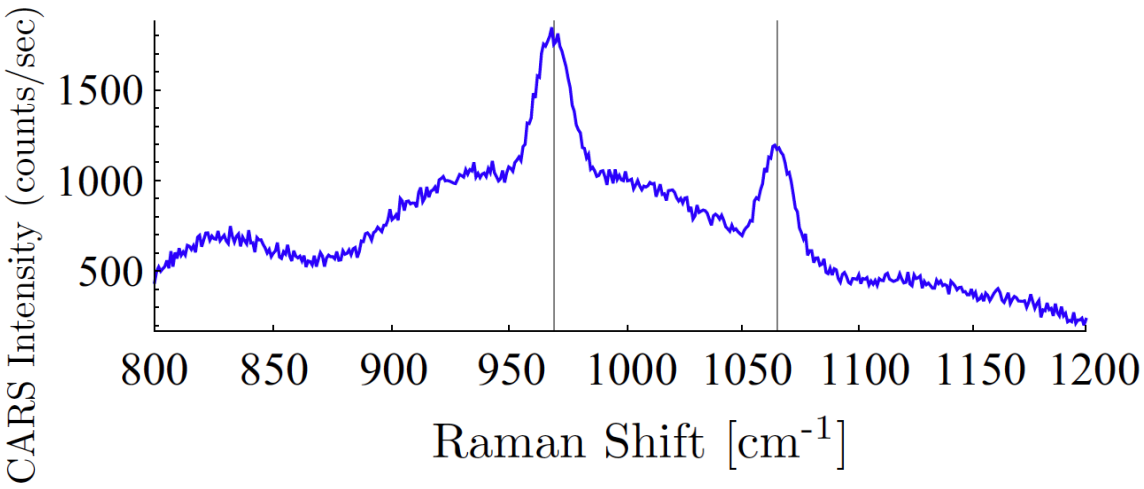

Figure 37 Experimental SECARS spectra of pyridazine on random gold NP aggregates from different focal spots on the sample. SECARS spectra showed two peaks.

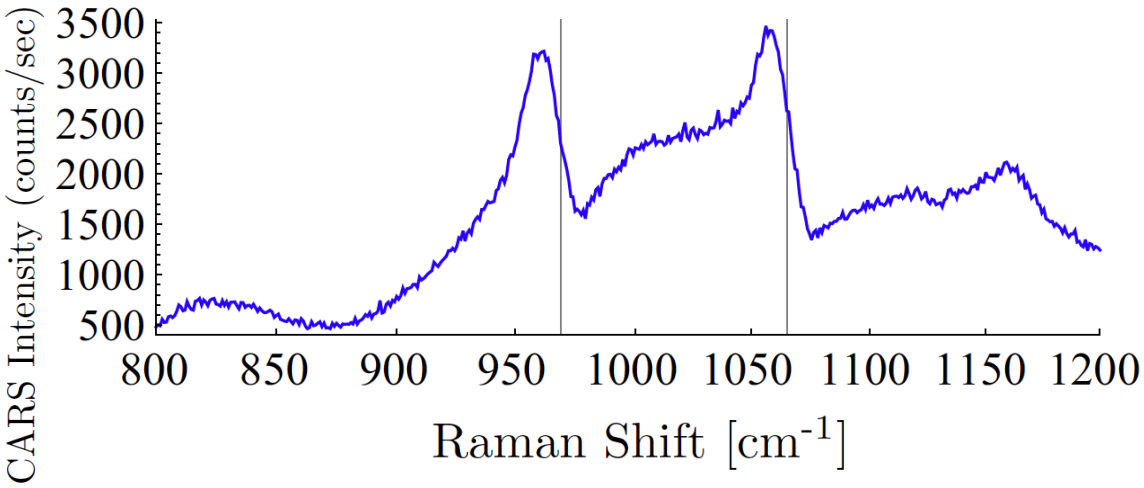

Figure 38 Experimental SECARS spectra of pyridazine on random gold NP aggregates from different focal spots on the sample. SECARS spectra showed intermediate shapes between two peaks and two dips.

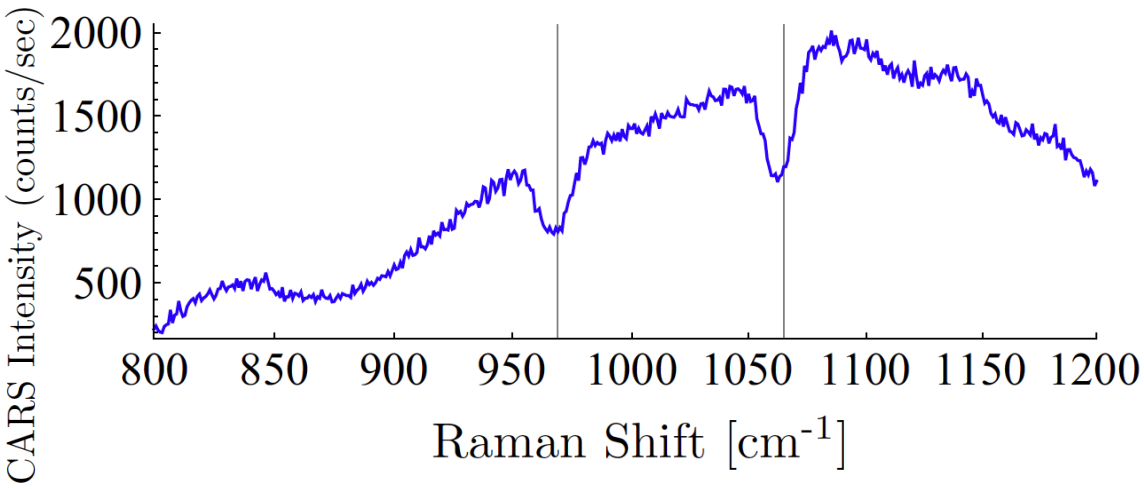

Figure 39 Experimental SECARS spectra of pyridazine on random gold NP aggregates from different focal spots on the sample. SECARS spectra showed two dips.

The experimental results are shown in Figure 37 - Figure 39. SECARS spectra were measured with laser beams focused on different spots on the sample. All three laser pulses (pump, Stokes, and probe) were overlapped in time. Therefore, the nonresonant background was not suppressed. The power of the beams at the sample was 50, 50, and 100 μW for the pump, Stokes, and probe, respectively. No visible damage or loss of signal over the time period of several hours was observed. No CARS signal was obtained from bulk pyridazine between two glass slides without gold NPs. However, strong SECARS signals were observed in the presence of gold NPs. The positions of the pyridazine spectral lines (vertical lines in Figure 37 - Figure 39) agreed with previous measurements of the vibrational spectra [100, 101]. The resulting SECARS spectra showed peaks (Figure 37),

dips (Figure 39), and intermediate shapes (Figure 38) which depend on the spatial position of the focused laser beams on the sample. The intermediate shapes were more frequently observed. Different spectral shapes observed at different spots demonstrate the local phase effects of the gold NP aggregates, which have different phase profiles, $\phi(r)$, as shown schematically in Figure 36 due to different responses to the incident laser fields. Many nanosize hot spots with different local phases contribute to the averaged CARS signals collected from the illuminated ~ 10 μm spot on the sample. These nano hot spots interfere and generate the total phase, which varies from one spot to another. The measured SECARS spectral shape depends on the relative phase between the local fields and the background. If the background is absent (e.g., suppressed by pulse shaping), only the peaks are observed (not shown). However, the SECARS signals from different hot spots still interfere, decreasing the overall EF. Here, we use the background to reveal the presence of these interferences via the measurements of the spatial dependence of the shape of SECARS spectra. We estimated the measured $EFs \sim 4-6\times10^{7}$ using the approach described in chapter III.

IV.C. Simulations

To better understand the spatial behavior of the SECARS spectra, we used a simplified model of gold NP aggregates by multiplying the pump, Stokes, and probe electric fields by Lorentzian response functions whose amplitudes and phases were scanned in the range of ~ 550–950 nm. Gaussian laser pulse shapes

$E_j(\omega) = \exp[-2\ln(2)(\frac{\omega - \omega_{j0}}{\Delta\omega_j})^2]$ were used to induce the CARS signals, where $j = 1, 2$ stands for pump and Stokes, respectively. ω_{j0} is the center frequency of the jth pulse, and $\Delta\omega_j$ is the corresponding bandwidth. The picosecond probe pulse was modeled by $E_{pr}(\omega) = 1$ if $\left|\omega - \omega_{pr}\right| / \alpha \le 5$ cm^{-1}, and 0 otherwise, where $\alpha = 2\pi c$ and c is the speed of light.

The nanoparticle response was modeled by a Lorentzian function [102], and the local field enhancement was given by

$$F(\omega') = 1 + \frac{A_{EF}\Delta}{\Omega_R - \omega' - i\Delta}, \quad (4)$$

where Ω_R is the SPR frequency, Δ is the half-width at half maximum (HWHM) of the Lorentzian, and AEF is the local field enhancement factor. The unity term in Eq. (4) accounts for the incident electric field.

The third-order nonlinear polarization was modeled by [73]

$$P^{(3)}(\omega) = \int_0^\infty [\chi_{NR}^{(3)}(\Omega) S_{12,NR}(\Omega) + \chi_R^{(3)}(\Omega) F(\omega - \Omega) \times S_{12,R}(\Omega)] E_3(\omega - \Omega) d\Omega, \quad (5)$$

where $\chi_R^{(3)}$, the resonant third-order nonlinear susceptibility, is given by

$$\chi_R^{(3)}(\omega') = \sum_k \frac{A_k \Gamma_k}{\Omega_{Rk} - \omega' - i\Gamma_k}, \quad (6)$$

$S_{12,NR}$ is

$$S_{12,NR}(\Omega) = \int_0^\infty E_1(\omega'') E_2^*(\omega'' - \Omega) d\omega'', \quad (7)$$

and $S_{12,R}$ is

$$S_{12,R}(\Omega) = \int_0^\infty F(\omega'')E_1(\omega'')F^*(\omega''-\Omega)E_2^*(\omega''-\Omega)d\omega'' . \quad (8)$$

A_k is a constant related to the Raman cross section, Γ_k gives the Raman line halfwidth (~1 cm^{-1}) [103], Ω_{Rk} is the *k*th molecular vibrational resonance frequency, and the asterisk denotes complex conjugate. The SECARS signal intensity is given by $I_{CARS}(\omega) \propto \left|P^{(3)}(\omega)\right|^2$. The simulations were performed in MATHEMATICA 8.

The simulation results are shown in Figure 40 - Figure 45. Two vibrational lines of pyridazine were chosen at ~ 968 and 1064 cm^{-1} based on the experimental values. The SECARS spectra were simulated using a Lorentzian response with $\Delta \sim 200$ cm^{-1}, A_{EF} = 10, and three values of the SPR wavelength at 672, 751, and 802 nm. The corresponding SECARS spectra are shown in Figure 40, Figure 42 and Figure 44, respectively. The incident electric field spectral amplitudes and the response amplitudes and phases are shown for these three cases in Figure 41, Figure 43 and Figure 45, respectively. The response phase (purple dashed) varies from 0 to π across the SPR and goes back to 0 at longer wavelengths due to the vanishing contribution of the Lorentzian response to the local field enhancement $F(\omega)$ as shown in Eq. (4). The total phase of the field is therefore equal to the phase of the incident field at longer wavelengths. During the scan of the SPR frequency, the phase of the SECARS signals also changed from 0 to π. This caused interference of the signals with the background and transformed SECARS peaks into dips (Figure 40, Figure 42 and Figure 44). The phase of the background was kept zero. This corresponds to the phase of the incident fields. Peaks, dips, and intermediate shapes of the SECARS spectra simulated using a simplified model in Figure 40, Figure 42 and Figure

44 are in agreement with those obtained in the experiments on a more complicated system in Figure 37 - Figure 39. The model gives insight into the mechanism of SECARS and allows describing the main spectral features using realistic parameters. For example, the chosen SPR and laser pulse frequencies coincide with the experimental values [96].

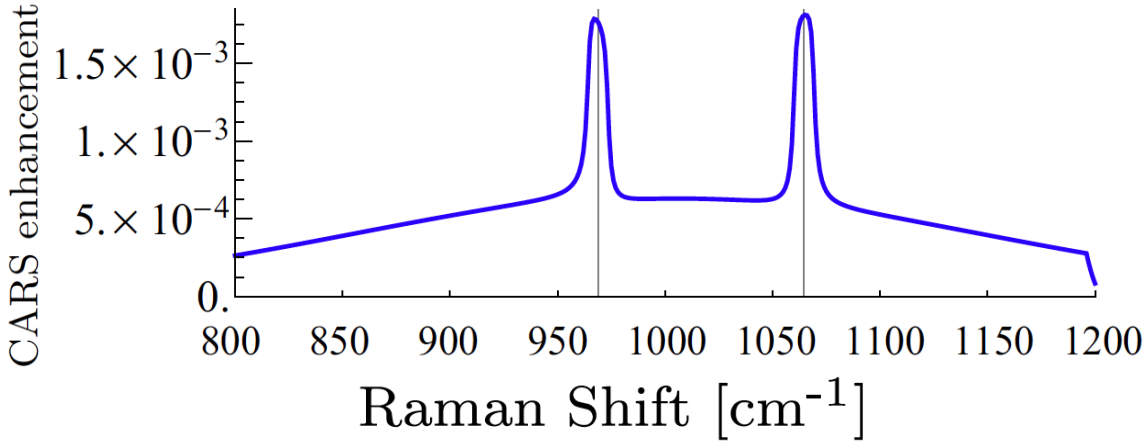

Figure 40 SECARS spectra of pyridzazine simulated with a Lorentzian response with HWHM Δ~$200cm^{-1}$, local field enhancement $A_{EF} = 10$ and SPR wavelength at 672 nm.

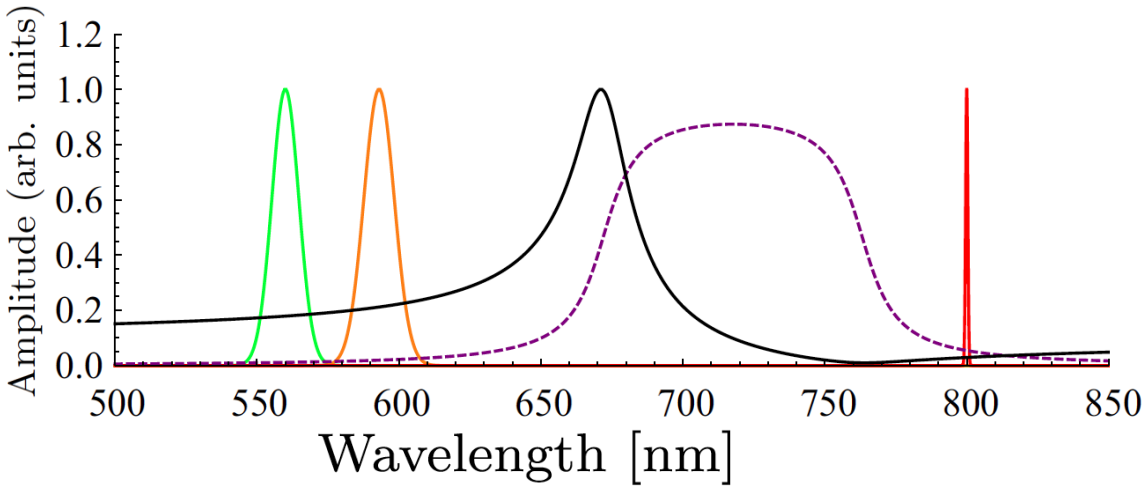

Figure 41 The electric field spectral amplitudes of the incident pump (green), Stokes (orange), and probe (red) laser pulses with normalized amplitude (solid black) and phase (purple dashed) of the local field enhancement $F(\omega)$, corresponding to the SPR wavelength at 672 nm.

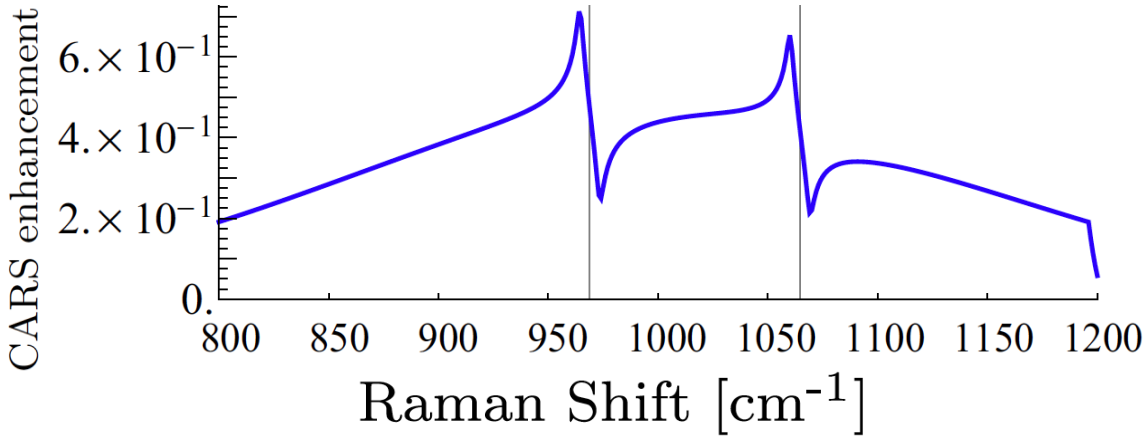

Figure 42 SECARS spectra of pyridzazine simulated with a Lorentzian response with HWHM Δ~$200cm^{-1}$, local field enhancement $A_{EF} = 10$ and SPR wavelength at 751 nm.

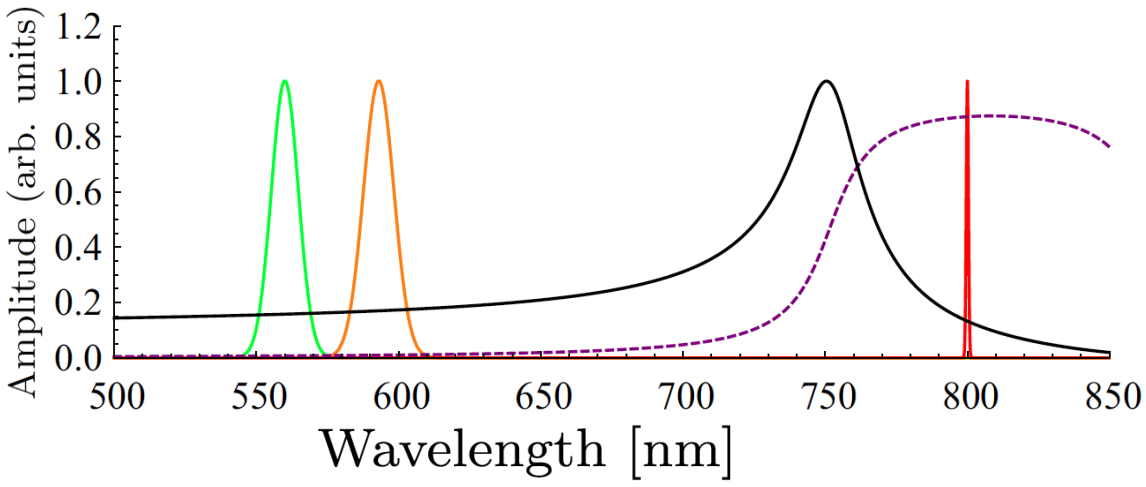

Figure 43 The electric field spectral amplitudes of the incident pump (green), Stokes (orange), and probe (red) laser pulses with normalized amplitude (solid black) and phase (purple dashed) of the local field enhancement $F(\omega)$, corrosponding to the SPR wavelength at 751 nm.

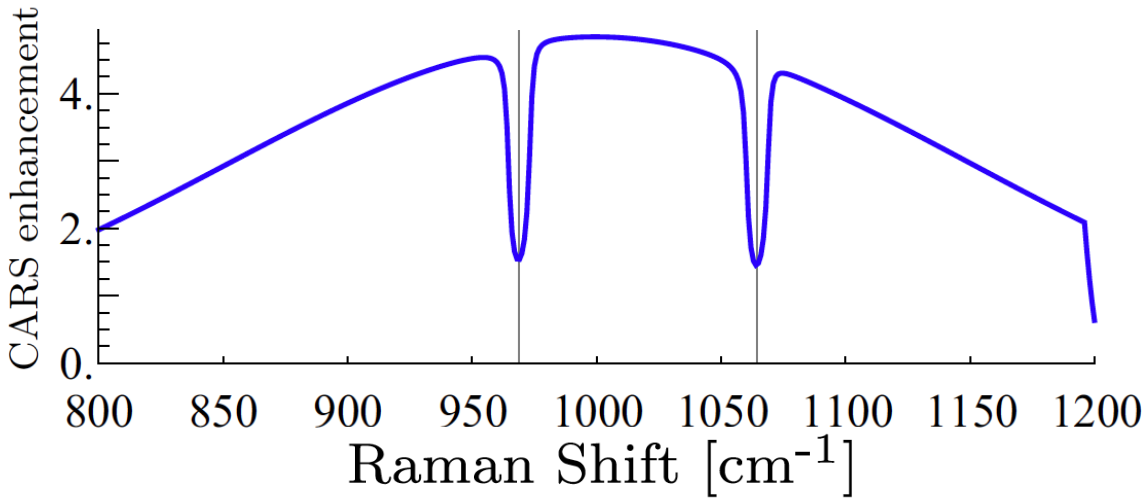

Figure 44 SECARS spectra of pyridzazine simulated with a Lorentzian response with HWHM Δ~$200cm^{-1}$, local field enhancement $A_{EF}=10$ and SPR wavelength at 802 nm.

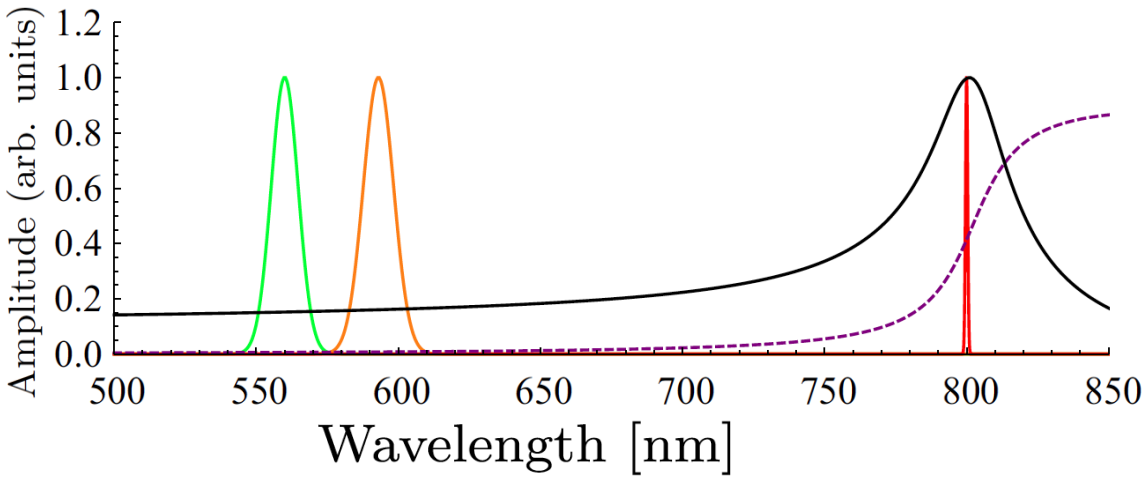

Figure 45 The electric field spectral amplitudes of the incident pump (green), Stokes (orange), and probe (red) laser pulses with normalized amplitude (solid black) and phase (purple dashed) of the local field enhancement $F(\omega)$, corresponding to the SPR wavelength at 802 nm.

The model also gives insight into the signal enhancement. The CARS enhancement in Figure 40, Figure 42 and Figure 44 was calculated by comparing CARS signals with and without the Lorentzian response, i.e., with $A_{EF} = 10$ and $A_{EF} = 0$, respectively. The SECARS EFs are plotted on the y axes of Figure 40, Figure 42 and Figure 44. Small and even negative EFs are obtained. This is due to the fact that the local field enhancement $F(\omega)$ in Eq. (4) is close to zero in a range of frequencies where the amplitude of the Lorentzian is approximately unity and the phase is π. In other words, the local field of the nanostructure can interfere destructively with the incident field and lead to suppression instead of enhancement of the CARS signals, generating "cold spots" instead of "hot

spots." The dip in the $F(\omega)$ profile (solid black) is clearly seen in Figure 41 around 750 nm in the vicinity of the CARS signal and the probe pulse. This leads to the smallest EF $\sim 10^{-3}$ shown in Figure 40.

IV.D. Discussion

The spatially resolved changes in SECARS interfering signals may be observed after averaging if one type of hot spots dominates in a particular excitation region. This is expected because the hot spots have different amplitudes and depending on the geometry some may be stronger than others. Two typical experimental SECARS spectra in Figure 46 show peak (blue) and dip (red) patterns at different spots on the sample. These spectra are averages over a distribution of hot spots within the laser focus. Increasing the focal diameter leads to further averaging and decreases the EF. Figure 46 shows the results of averaging over ten spots (black). A dramatic signal suppression is observed. The simplified model reveals a similar behavior. Figure 47 shows two typical spectra with SPRs centered at 672 and 802 nm resulting in peaks (blue) and dips (red), respectively. Averaging over four spectra with SPRs at 672, 751, 802, and 892 nm results in a suppressed signal (black) in Figure 47.

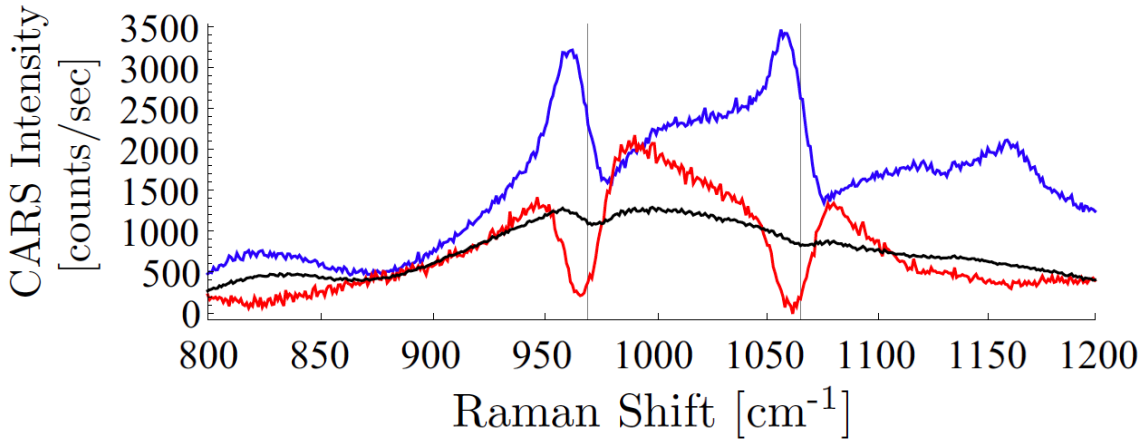

Figure 46 Experimental SECARS spectra of pyridazine: peaks (blue), dips (red), and averaged (black) spectra. Ten spots were averaged. Averaging decreased the SECARS signal magnitude.

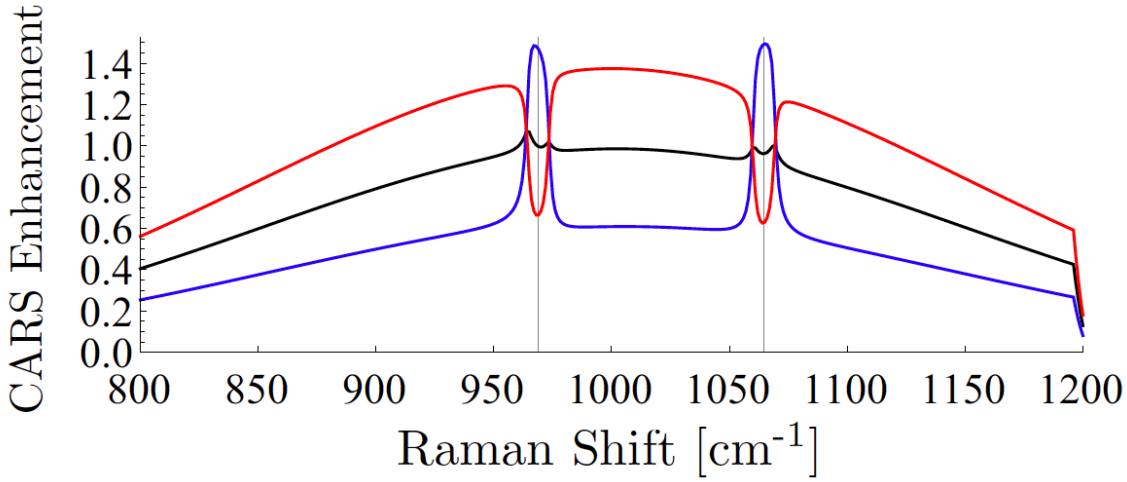

Figure 47 Simulated SECARS spectra of pyridazine: peaks (blue), dips (red), and averaged (black) spectra. Four spots were averaged. Averaging decreased the SECARS signal magnitude.

In the experiments, many hot spots are expected to contribute to the measured SECARS signals due to the high roughness of the surface and availability of a large number of closely spaced nanoparticles. The measured signals have the averaged phase which can reveal the averaged information on the statistical distribution of different kinds of hot spots within the excitation region. This distribution of different phases leads to destructive interference and decreases the magnitude of the CARS signals. We consider this phase effect as the primary source of the discrepancy between the predicted large and the observed small EFs. This problem may be addressed by laser pulse shaping. Here we used unshaped incident Gaussian laser pulses. Adaptive [104, 105] and deterministic [66, 106] near-field control methods may be used to compensate these phase effects and minimize destructive interference.

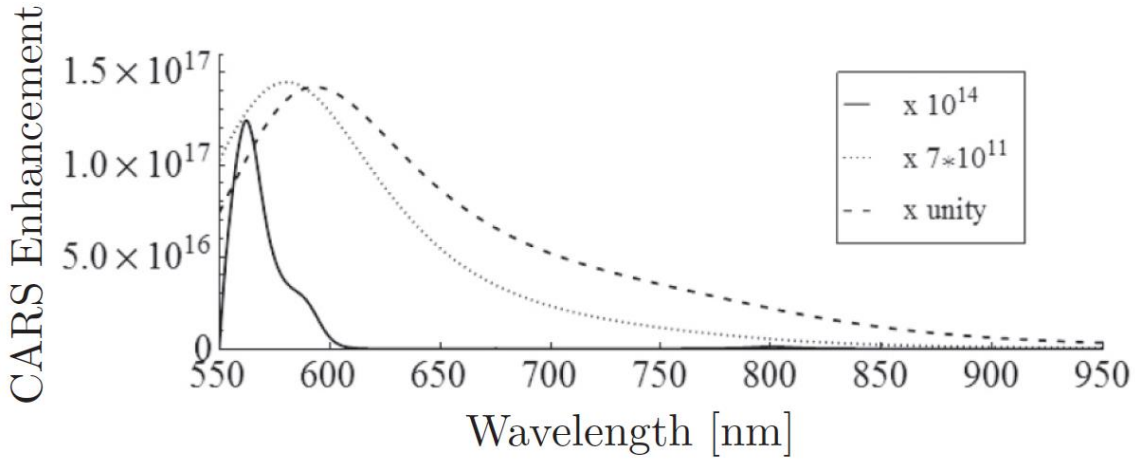

Figure 48 Simulated CARS enhancement as a function of SPR frequency for different SPR linewidth and local field enhancement: (Solid) $\Delta = 201.6cm^{-1}$, $A_{EF} = 10$; (dotted) $\Delta = 2016cm^{-1}$, $A_{EF} = 10$; (Dashed) $\Delta = 2016cm^{-1}$, $A_{EF} = 1000$. Legend shows scale factors multiplied to the data to fit curves on graph.

Another effect, which contributes to the CARS enhancement, is the spatial mode overlap of the local electric fields enhanced by plasmonic nanostructures. We investigate this effect by simulating SECARS signals as a function of the SPR frequency and linewidth. Figure 48 shows the simulated CARS enhancement of the 968 cm^{-1} line of pyridazine for different SPR parameters: (solid) $\Delta = 201.6cm^{-1}$, $A_{EF} = 10$; (dotted) $\Delta = 2016cm^{-1}$, $A_{EF} = 10$; (dashed) $\Delta = 2016cm^{-1}$, $A_{EF} = 1000$. These plots show optimal SPR frequencies to achieve the maximum CARS enhancement for the specific arrangement of laser pulse configurations used in the experiments. The distribution of SPR frequencies in random gold NP aggregates further reduces the CARS EFs and should be taken into account when designing the substrates and laser pulse configurations. The SPR linewidth $\Delta = 2016cm^{-1}$ corresponds to single NPs [107] and the reduced $\Delta = 201.6cm^{-1}$ to NP aggregates. SPRs of complex nanostructures can be described as Lorentzian oscillators with the number of Lorentzians, near-field EFs, and linewidths varying depending on the nanostructure geometry. The broad SPR spectrum in Figure 21 is an average over many hot spots with different linewidths. Each particular hot spot has a narrower linewidth than the average. Therefore, the observed EFs may be further reduced due to the challenge of matching the three CARS pulse center frequencies to the plasmonic resonances.

The gold film is not uniform with an average thickness of 500–800 nm measured by AFM, and is better described as a collection of diffusion-limited fractal-like aggregates with various SPRs. Larger values of A_{EF} also correspond to NP aggregates and to

specially designed plasmonic substrates. Figure 48 shows that for $A_{EF} = 1000$ and $\Delta = 2016 cm^{-1}$, the CARS enhancement of EF $\sim 10^{17}$ may be obtained. To achieve such EFs in experiments, one has to take into account the local phase effects described above. One approach is to use high quality periodic substrates with a narrow distribution of SPR linewidths and frequencies [52]. As an example, we considered a periodic array of cross-dipole nanoantennas made of gold strips of 43 nm length, 10nm width, and 10nm height with$\sim$ 128 near-field enhancement above the dipole gap in the plane 15 nm above the surface [108]. The corresponding SECARS EFs of $\sim 10^{11}$ and $\sim 10^{12}$ were calculated for these nanostructures with typical SPR linewidths of 140 and 230 meV, respectively.

IV.E. Conclusion

In summary, we provide insights into the nature of surface enhanced coherent nonlinear optical signal enhancement and investigate the dependence of surface-enhanced coherent Raman scattering on SPR parameters. We measured the spatial dependence of the SECARS spectra of pyridazine on random gold NP aggregates and used a simplified model to understand the experimental results. Similar effects may be present in SERS experiments. However, SERS is an incoherent technique and there is no FWM background that can reveal the local phases. We attribute the previously measured small SECARS EFs to destructive interference and SPR distribution effects, and report the first measurements of nanoscale phase effects in SECARS using the interference of the CARS signals and FWM background. This approach provides information about the local phase of the

nanostructures and may be extended to the subwavelength scale. We propose strategies to improve the signal enhancement by many orders of magnitude. Our results may be used to extend other related techniques such as FAST CARS [63] to the nanoscale.

CHAPTER V

CONCLUSIONS

This dissertation is a summary of part of my work did in my PhD study. In this dissertation, we explored the utility of Raman coherence in two sets of experiments. In chapter II, we generated multi-color optical vortices in a Raman-active crystal $PbWO_4$ using two-color femtosecond laser pulses. We focusing an OAM containing pump beam and a femtosecond Stokes beam into a Raman-active crystal and generated many orders of multi-color OV beams. We have shown that the OVs are sensitive to the pulse energy, beam diameter as well as the spatial-temporal overlaps of the beam. We measured the TC of the OVs using two methods – a tilted lens and an interferometer to measure the TC of the OVs and found that the generated OVs follow OAM transfer in a way similar to frequency conversion. The interference fringes of the OV beams and Gaussian reference beam show that the high-order OVs generated inside Raman crystals are unstable and split in to several charge 1 OVs. These vortices, in principle, could support a 3.5 fs vortex beam, if spatially and temporally combined with proper phases.

In chapter III, we explore detection and sensing applications. Three laser beams, pump, Stokes and probe, are focused in to Raman molecules. Under certain conditions, a fourth beam, CARS will be generated. We attached the Raman molecules to a rough gold nanoparticle surface and achieved further improvement of efficiency by using field enhancement due to surface plasmon resonances in aggregates of gold nanoparticles. We shaped the probe pulse into a picosecond pulse with Sinc profile. We scan the time delay

of the probe pulse to get the time resolved spectra information. This new vibrational spectroscopic technique is called time-resolved surface-enhanced coherent anti-Stokes Raman scattering (tr-SECARS). We used tr-SECARS to obtain the Raman spectra information of hydrogen-bonded molecular complexes of pyridine with water in the near field of gold nanoparticles. When spectra resolution is not high enough, the adjacent Raman modes will congestion. We analyze the temporal trace of the quantum beating of multiple Raman modes and identify the Raman modes of pyridine-water complex. The experiment demonstrated the sensitivity of the tr-SECARS technique and confirmed the existence of the pyridine-water complex in our pyridine sample. We analyze the surface enhancement due to the gold nanoparticle surface and get the enhancement factor is about 10^7.

In the chapter IV, we discuss the discrepancy in SECARS enhancement factors, observed in the experiment and calculated theoretically. We measured the spatial dependence of the SECARS spectra of pyridazine on random gold NP aggregates and used a simplified model to understand the experimental results. We attribute the previously measured small SECARS EFs to destructive interference and SPR distribution effects, and report the first measurements of nanoscale phase effects in SECARS using the interference of the CARS signals and FWM background.

REFERENCES

1. Raman, C.V. and Krishnan, K.S., *A new type of secondary radiation.* Nature, 1928. **121**: p. 501-502.
2. Bloember, N., *Stimulated Raman effect.* American Journal of Physics, 1967. **35**(11): p. 989-1023.
3. Begley, R.F., Harvey, A.B., and Byer, R.L., *Coherent anti-Stokes Raman-spectroscopy.* Applied Physics Letters, 1974. **25**(7): p. 387-390.
4. Maker, P.D. and Terhune, R.W., *Study of optical effects due to an induced polarization third order in electric field strength.* Physical Review, 1965. **137**(3A): p. A801-818.
5. Kneipp, K., Moskovits, M., and Kneipp, H., *Surface-enhanced Raman scattering: physics and applications*. Topics in Applied Physics. Vol. 103. 2006, New York: Springer.
6. Fleischmann, M., Hendra, P.J., and Mcquilla, A.J., *Raman-spectra of pyridine adsorbed at a silver electrode.* Chemical Physics Letters, 1974. **26**(2): p. 163-166.
7. Lombardi, J.R. and Birke, R.L., *A unified approach to surface-enhanced Raman spectroscopy.* Journal of Physical Chemistry C, 2008. **112**(14): p. 5605-5617.
8. Lombardi, J.R. and Birke R.L., *A unified view of surface-enhanced Raman scattering.* Accounts of Chemical Research, 2009. **42**(6): p. 734-742.

9. Wessel, J., *Surface-enhanced optical microscopy.* Journal of the Optical Society of America B-Optical Physics, 1985. **2**(9): p. 1538-1541.

10. Le Ru, E.C. and Etchegoin, P.G., *Principles of surface-enhanced Raman spectroscopy: And Related Plasmonic Effects*. 2008, Amsterdam Oxford: Elsevier.

11. Schluecker, S. and Kiefer, W., *Surface enhanced Raman spectroscopy*. 2011, New York: Wiley.

12. Le Ru, E.C., Blackie, E., Meyer, M. and Etchegoin, P.G., *Surface enhanced Raman scattering enhancement factors: a comprehensive study.* Journal of Physical Chemistry C, 2007. **111**(37): p. 13794-13803.

13. Koo, T.W., Chan, S. and Berlin, A.A., *Single-molecule detection of biomolecules by surface-enhanced coherent anti-Stokes Raman scattering.* Optics Letters, 2005. **30**(9): p. 1024-1026.

14. Le Ru, E.C. and Etchegoin, P.G., *Single-molecule surface-enhanced Raman spectroscopy.* Annual Review of Physical Chemistry, 2012. **63**: p. 65-87.

15. Nie, S.M. and Emory, S.R., *Single-molecule detection and spectroscopy by surface-enhanced Raman scattering.* Abstracts of Papers of the American Chemical Society, 1997. **213**: p. 177-PHYS.

16. Yao, A.M. and Padgett, M.J., *Orbital angular momentum: origins, behavior and applications.* Advances in Optics and Photonics, 2011. **3**(2): p. 161-204.

17. Fazal, F.M. and Block, S.M., *Optical tweezers study life under tension.* Nature Photonics, 2011. **5**(6): p. 318-321.

18. Okulov, A.Y., *Cold matter trapping via slowly rotating helical potential.* Physics Letters A, 2012. **376**(4): p. 650-655.

19. Neupane, B., Chen, F., Sun, W., Chiu, D.T. and Wang, G.F., *Tuning donut profile for spatial resolution in stimulated emission depletion microscopy.* Review of Scientific Instruments, 2013. **84**(4): p. 043701.

20. Robb, G.R.M., *Superradiant exchange of orbital angular momentum between light and cold atoms.* Physical Review A, 2012. **85**(2): p. 023426.

21. Padgett, M.J., *Light in a twist: optical angular momentum.* Proc. SPIE, 2013. **8637**: p. 863702.

22. Hnatovsky, C., Shvedovm V.G., Krolikowski, W. and Rode, A.V., *Materials processing with a tightly focused femtosecond laser vortex pulse.* Optics Letters, 2010. **35**(20): p. 3417-3419.

23. Toyoda, K., Miyamoto, K., Aoki, N., Morita, R. and Omatsu, T., *Using optical vortex to control the chirality of twisted metal nanostructures.* Nano Letters, 2012. **12**(7): p. 3645-3649.

24. Vasnetsov, M. and Staliunas, K., *Interaction of optical vortices in nonlinear crystals*, in *Optical vortices*. 1999, Hauppauge: Nova Science Publishers.

25. Yusufu, T., Tokizane, Y., Yamada, M., Miyamoto, K. and Omatzu, T., *Tunable 2-μm optical vortex parametric oscillator.* Optics Express, 2012. **20**(21): p. 23666-23675.

26. Lenzini, F., Residori, S., Arecchi, F.T. and Bortolozzo, U., *Optical vortex interaction and generation via nonlinear wave mixing.* Physical Review A, 2011. **84**(6).

27. Dholakia, K., Simpson, N.B., Padgett, M.J. and Allen, L., *Second-harmonic generation and the orbital angular momentum of light.* Physical Review A, 1996. **54**(5): p. R3742-R3745.

28. Bovino, F.A., Braccini, M. Giardina, M. and Sibilia, C., *Orbital angular momentum in noncollinear second-harmonic generation by off-axis vortex beams.* Journal of the Optical Society of America B-Optical Physics, 2011. **28**(11): p. 2806-2811.

29. Bezuhanov, K., Dreischuh, A., Paulus, G.G., Schatzel, M.G. and Walther, H., *Vortices in femtosecond laser fields.* Optics Letters, 2004. **29**(16): p. 1942-1944.

30. Mariyenko, I.G., Strohaber, J., and Uiterwaal, C.J.G.J., *Creation of optical vortices in femtosecond pulses.* Optics Express, 2005. **13**(19): p. 7599-7608.

31. Strohaber, J., Petersen, C., and Uiterwaal, C.J.G.J., *Efficient angular dispersion compensation in holographic generation of intense ultrashort paraxial beam modes.* Optics Letters, 2007. **32**(16): p. 2387-2389.

32. Chan, H.S., Hsieh, Z.M., Liang, W.H., Kung, A.H., Lee, C.K., et al., *Synthesis and measurement of ultrafast waveforms from five discrete optical harmonics.* Science, 2011. **331**(6021): p. 1165-1168.

33. Sokolov, A.V., Shverdin, M.Y., Walker, D.R., Yavuz, D.D., Burzo, A.M., et al., *Generation and control of femtosecond pulses by molecular modulation.* Journal of Modern Optics, 2005. **52**(2-3): p. 285-304.

34. Zhi, M.C. and Sokolov, A.V., *Toward single-cycle pulse generation in Raman-active crystals.* Ieee Journal of Selected Topics in Quantum Electronics, 2012. **18**(1): p. 460-466.

35. Strohaber, J., Zhi, M.C., Sokolov, A.V., Kolomenskii, A.A., Paulus, G.G., et al., *Coherent transfer of optical orbital angular momentum in multi-order Raman sideband generation.* Optics Letters, 2012. **37**(16): p. 3411-3413.

36. Zhi, M.C., Wang, K., Hua, X. and Sokolov, A.V., *Pulse-shaper-assisted phase control of a coherent broadband spectrum of Raman sidebands.* Optics Letters, 2011. **36**(20): p. 4032-4034.

37. Gorbach, A.V., Skryabin, D.V. and Harvey, C.N., *Vortex solitons in an off-resonant Raman medium.* Physical Review A, 2008. **77**(6).

38. Zhi, M.C., Wang, K., Hua, X., Strycker, B.D. and Sokolov, A.V., *Shaper-assisted phase optimization of a broad "holey" spectrum.* Optics Express, 2011. **19**(23): p. 23400-23407.

39. Zhi, M.C., Wang, K. and Sokolov, A.V., *Toward single-cycle pulse generation in single-crystal diamond*, in *17th International conference on ultrafast phenomena*. 2010: Snowmass, Colorado.

40. Oemrawsingh, S.S.R., van Houwelingen, J.A.W., Eliel, E.R., Woerdman, J.P., Verstegen, E.J.K., et al., *Production and characterization of spiral phase plates for optical wavelengths.* Applied Optics, 2004. **43**(3): p. 688-694.

41. Zhi, M.C., Wang, X. and Sokolov, A.V., *Broadband coherent light generation in diamond driven by femtosecond pulses.* Optics Express, 2008. **16**(16): p. 12139-12147.

42. Anderson, M.E., Bigman, H., de Araujo, L.E.E. and Chaloupka, J.L., *Measuring the topological charge of ultrabroadband, optical-vortex beams with a triangular aperture.* Journal of the Optical Society of America B-Optical Physics, 2012. **29**(8): p. 1968-1976.

43. Guo, C.S., Lu, L.L. and Wang, H.T., *Characterizing topological charge of optical vortices by using an annular aperture.* Optics Letters, 2009. **34**(23): p. 3686-3688.

44. Vaity, P., Banerji, J. and Singh, R.P., *Measuring the topological charge of an optical vortex by using a tilted convex lens.* Physics Letters A, 2013. **377**(15): p. 1154-1156.

45. Ricci, F., Loffler, W. and van Exter, M.P., *Instability of higher-order optical vortices analyzed with a multi-pinhole interferometer.* Optics Express, 2012. **20**(20): p. 22961-22975.

46. Minck, R.W., Terhune, R.W. and Rado, W.G., *Laser-stimulated Raman effect and resonant 4-photon interactions in gases H_2, D_2, and CH_4.* Applied Physics Letters, 1963. **3**(10): p. 181-184.

47. Addison, C.J., Konorov, S.O., Brolo, A.G., Blades, M.W. and Turner, R.F.B., *Tuning gold nanoparticle self-assembly for optimum coherent anti-Stokes Raman scattering and second harmonic generation response.* Journal of Physical Chemistry C, 2009. **113**(9): p. 3586-3592.

48. Hayazawa, N., Ichimura, T., Hashimoto, M., Inouye, Y. and Kawata, S., *Amplification of coherent anti-Stokes Raman scattering by a metallic nanostructure for a high resolution vibration microscopy.* Journal of Applied Physics, 2004. **95**(5): p. 2676-2681.

49. Ichimura, T., Hayazawa, N., Hashimoto, M., Inouye, Y. and Kawata, S., *Tip-enhanced coherent anti-Stokes Raman scattering for vibrational nanoimaging.* Physical Review Letters, 2004. **92**(22).

50. Liang, E.J., Weippert, A., Funk, J.M., Materny, A. and Kiefer, W., *Experimental observation of surface-enhanced coherent anti-Stokes Raman scattering.* Chemical Physics Letters, 1994. **227**(1-2): p. 115-120.

51. Namboodiri, V., Namboodiri, M., Diaz, G.I.C., Oppermann, M., Flachenecker, G., et al., *Surface-enhanced femtosecond CARS spectroscopy (SE-CARS) on pyridine.* Vibrational Spectroscopy, 2011. **56**(1): p. 9-12.

52. Steuwe, C., Kaminski, C.F., Baumberg, J.J. and Mahajan, S., *Surface enhanced coherent anti-Stokes Raman scattering on nanostructured gold surfaces.* Nano Letters, 2011. **11**(12): p. 5339-5343.

53. Wang, Y., Lin, C.Y., Nikolaenko, A., Raghunathan, V. and Potma, E.O., *Four-wave mixing microscopy of nanostructures.* Advances in Optics and Photonics, 2011. **3**(1): p. 1-52.

54. Berg, E.R., Freeman, S.A., Green, D.D. and Ulness, D.J., *Effects of hydrogen bonding on the ring stretching modes of pyridine.* Journal of Physical Chemistry A, 2006. **110**(50): p. 13434-13446.

55. Schlucker, S., Heid, M., Singh, R.K., Asthana, B.P., Popp, J., et al., *Vibrational dynamics in hydrogen-bonded (pyridine plus water) complexes studied by spectrally resolved femtosecond CARS.* Zeitschrift Fur Physikalische Chemie-International Journal of Research in Physical Chemistry & Chemical Physics, 2002. **216**: p. 267-278.

56. Schlucker, S., Singh, R.K., Asthana, B.P., Popp, J. and Kiefer, W., *Hydrogen-bonded pyridine-water complexes studied by density functional theory and raman spectroscopy.* Journal of Physical Chemistry A, 2001. **105**(43): p. 9983-9989.

57. Addison, C.J. and Brolo, A.G., *Nanoparticle-containing structures as a substrate for surface-enhanced Raman scattering.* Langmuir, 2006. **22**(21): p. 8696-8702.

58. Anema, J.R., Brolo, A.G., Felten, A. and Bittencourt, C., *Surface-enhanced Raman scattering from polystyrene on gold clusters.* Journal of Raman Spectroscopy, 2010. **41**(7): p. 745-751.

59. Pestov, D., Murawski, R.K., Ariunbold, G.O., Wang, X., Zhi, M.C., et al., *Optimizing the laser-pulse configuration for coherent Raman spectroscopy.* Science, 2007. **316**(5822): p. 265-268.

60. Pestov, D., Wang, X., Ariunbold, G.O., Murawski, R.K., Sautenkov, V.A., et al., *Single-shot detection of bacterial endospores via coherent Raman spectroscopy.* Proceedings of the National Academy of Sciences of the United States of America, 2008. **105**(2): p. 422-427.

61. Daniel, M.C. and Astruc, D., *Gold nanoparticles: Assembly, supramolecular chemistry, quantum-size-related properties, and applications toward biology, catalysis, and nanotechnology.* Chemical Reviews, 2004. **104**(1): p. 293-346.

62. Elghanian, R., Storhoff, J.J., Mucic, R.C., Letsinger, R.L. and Mirkin, C.A., *Selective colorimetric detection of polynucleotides based on the distance-dependent optical properties of gold nanoparticles.* Science, 1997. **277**(5329): p. 1078-1081.

63. Scully, M.O., Kattawar, G.W., Lucht, R.P., Opatrny,T., Pilloff, H., et al., *FAST CARS: Engineering a laser spectroscopic technique for rapid identification of bacterial spores.* Proceedings of the National Academy of Sciences of the United States of America, 2002. **99**(17): p. 10994-11001.

64. Choi, D.S., Jeoung, S.C. and Chon, B.H., *Thickness dependent CARS measurement of polymeric thin films without depth-profiling.* Optics Express, 2008. **16**(4): p. 2604-2613.

65. Chew, H., Wang, D.S. and Kerker, M., *Surface enhancement of coherent anti-Stokes Raman scattering by colloidal spheres.* Journal of the Optical Society of America B-Optical Physics, 1984. **1**(1): p. 56-66.

66. Aeschlimann, M., Bauer, M., Bayer, D., Brixner, T., Cunovic, S., et al., *Optimal open-loop near-field control of plasmonic nanostructures.* New Journal of Physics, 2012. **14**.

67. Aeschlimann, M., Bauer, M., Bayer, D., Brixner, T., Cunovic, S., et al., *Spatiotemporal control of nanooptical excitations.* Proceedings of the National Academy of Sciences of the United States of America, 2010. **107**(12): p. 5329-5333.

68. Muhlschlegel, P., Eisler, H.J., Martin, O.J.F., Hecht, B. and Pohl, D.W., *Resonant optical antennas.* Science, 2005. **308**(5728): p. 1607-1609.

69. Huang, J.S., Voronine, D.V., Tuchscherer, P., Brixner, T. and Hecht, B., *Deterministic spatiotemporal control of optical fields in nanoantennas and plasmonic circuits.* Physical Review B, 2009. **79**(19).

70. Parkhill, J.A., Rappoport, D. and Aspuru-Guzik, A., *Modeling coherent anti-stokes Raman Scattering with time-dependent density functional theory: Vacuum and surface enhancement.* Journal of Physical Chemistry Letters, 2011. **2**(15): p. 1849-1854.

71. Genevet, P., Tetienne, J.P., Gatzogiannis, E., Blanchard, R., Kats, M.A., et al., *Large enhancement of nonlinear optical phenomena by plasmonic nanocavity gratings.* Nano Letters, 2010. **10**(12): p. 4880-4883.

72. Aeschlimann, M., Brixner, T., Fischer, A., Kramer, C., Melchior, P., et al., *Coherent two-dimensional nanoscopy.* Science, 2011. **333**(6050): p. 1723-1726.

73. Mukamel, S., *Principles of nonlinear optical spectroscopy*. 1999, New York: Oxford University Press.

74. Lee, Y., Martin, C.D., Parise, J.B., Hriljac, J.A. and Vogt, T., *Formation and manipulation of confined water wires.* Nano Letters, 2004. **4**(4): p. 619-621.

75. Chung, C.Y., Boik, J. and Potma, E.O., *Biomolecular imaging with coherent nonlinear vibrational microscopy.* Annual Review of Physical Chemistry, 2013. **64**: p. 77-99.

76. Zumbusch, A., Holtom, G.R. and Xie, X.S., *Three-dimensional vibrational imaging by coherent anti-Stokes Raman scattering.* Physical Review Letters, 1999. **82**(20): p. 4142-4145.

77. Cheng, J.X. and Xie, X.S., *Coherent Raman scattering microscopy*. 2013, Boca Raton, FL: CRC Press.

78. Cheng, J.X., Book, L.D. and Xie, X.S., *Polarization coherent anti-Stokes Raman scattering microscopy.* Optics Letters, 2001. **26**(17): p. 1341-1343.

79. Jurna, M., Korterik, J.P., Otto, C., Herek, J.L. and Offerhaus, H.L., *Vibrational phase contrast microscopy by sse of coherent anti-Stokes Raman scattering.* Physical Review Letters, 2009. **103**(4).

80. Potma, E.O., Evans, C.L. and Xie, X.S., *Heterodyne coherent anti-Stokes Raman scattering (CARS) imaging.* Optics Letters, 2006. **31**(2): p. 241-243.

81. Wang, X., Zhang, A.H., Zhi, M.C., Sokolov, A.V., Welch, G.R., et al., *Heterodyne coherent anti-Stokes Raman scattering for spectral phase retrieval and signal amplification.* Optics Letters, 2010. **35**(5): p. 721-723.

82. Ganikhanov, F., Evans, C.L., Saar, B.G. and Xie, X.S., *High-sensitivity vibrational imaging with frequency modulation coherent anti-Stokes Raman scattering (FM CARS) microscopy.* Optics Letters, 2006. **31**(12): p. 1872-1874.

83. Volkmer, A., Book, L.D. and Xie, X.S., *Time-resolved coherent anti-Stokes Raman scattering microscopy: Imaging based on Raman free induction decay.* Applied Physics Letters, 2002. **80**(9): p. 1505-1507.

84. Brinks, D., Hildner, R., Stefani, F.D. and van Hulst, N.F., *Beating spatio-temporal coupling: implications for pulse shaping and coherent control experiments.* Optics Express, 2011. **19**(27): p. 26486-26499.

85. van Rhijn, A.C.W., Jurna, M., Jafarpour, A., Herek, J.L. and Offerhaus, H.L., *Phase-shaping strategies for coherent anti-Stokes Raman scattering.* Journal of Raman Spectroscopy, 2011. **42**(10): p. 1859-1863.

86. Volpe, G., Cherukulappurath, S., Parramon, R.J., Molina-Terriza, G. and Quidant, R., *Controlling the optical near field of nanoantennas with spatial phase-shaped beams.* Nano Letters, 2009. **9**(10): p. 3608-3611.

87. Novotny, L. and Hecht, B., *Principles of nano-optics*. 2006, New York: Cambridge University Press.

88. Geddes, C.D., *Metal-enhanced fluorescence*. 2010, NewYork: Wiley.

89. Antoine, R., Brevet, P.F., Girault, H.H., Bethell, D. and Schiffrin, D.J., *Surface plasmon enhanced non-linear optical response of gold nanoparticles at the air/toluene interface.* Chemical Communications, 1997(19): p. 1901-1902.

90. Bouhelier, A., Beversluis, M., Hartschuh, A. and Novotny, L., *Near-field second-harmonic generation induced by local field enhancement.* Physical Review Letters, 2003. **90**(1): p. 013903.

91. Lippitz, M., van Dijk, M.A. and Orrit, M., *Third-harmonic generation from single gold nanoparticles.* Nano Letters, 2005. **5**(4): p. 799-802.

92. Chemla, D.S., Heritage, J.P., Liao, P.F. and Isaacs, E.D., *Enhanced 4-wave mixing from silver particles.* Physical Review B, 1983. **27**(8): p. 4553-4558.

93. Poutrina, E., Ciraci, C., Gauthier, D.J. and Smith, D.R., *Enhancing four-wave-mixing processes by nanowire arrays coupled to a gold film.* Optics Express, 2012. **20**(10): p. 11005-11013.

94. Chen, C.K., Castro, A.R.B.D., Shen, Y.R. and Demartini, F., *Surface coherent anti-Stokes Raman spectroscopy.* Physical Review Letters, 1979. **43**(13): p. 946-949.

95. Schlucker, S., Salehi, M., Bergner, G., Schutz, M., Strobel, P., et al., *Immuno-surface-enhanced coherent anti-Stokes Raman scattering microscopy: Immunohistochemistry with target-specific metallic nanoprobes and nonlinear Raman microscopy.* Analytical Chemistry, 2011. **83**(18): p. 7081-7085.

96. Voronine, D.V., Sinyukov, A.M., Hua, X., Wang, K., Jha, P.K., et al., *Time-resolved surface-enhanced coherent sensing of nanoscale molecular complexes.* Scientific Reports, 2012. **2**: p. 891.

97. Shalaev, V.M., *Nonlinear optics of random media*. 1999, New York: Springer.

98. Ichimura, T., Hayazawa, N., Hashimoto, M., Inouye, Y. and Kawata, S., *Local enhancement of coherent anti-Stokes Raman scattering by isolated gold nanoparticles.* Journal of Raman Spectroscopy, 2003. **34**(9): p. 651-654.

99. Kim, H.M., Xiang, C.X., Guell, A.G., Penner, R.M. and Potma, E.O., *Tunable two-photon excited luminescence in single gold nanowires fabricated by lithographically patterned nanowire electrodeposition.* Journal of Physical Chemistry C, 2008. **112**(33): p. 12721-12727.

100. Ozono, Y., Nibu, Y., Shimada, H. and Shimada, R., *Polarized Raman and infrared-spectra of [H-1(4)] pyridazines and [H-2(4)] pyridazines.* Bulletin of the Chemical Society of Japan, 1986. **59**(10): p. 2997-3001.

101. Stidham, H.D. and Tucci, J.V., *Vibrational spectra of pyridazine pyridazine-D4 pyridazine-3,6-D2 and pyridazine-4,5-D2.* Spectrochimica Acta Part a-Molecular Spectroscopy, 1967. **A 23**(8): p. 2233-&.

102. Bohren, C.F. and Huffman, D.R., *Absorption and scattering of light by small particles*. 2007, New York: Wiley.

103. Vazquez, J., Gozalez, J.J.L., Marquez, F. and Boggs, J.E., *Vibrational spectrum of pyridazine.* Journal of Raman Spectroscopy, 1998. **29**(6): p. 547-559.

104. Aeschlimann, M., Bauer, M., Bayer, D., Brixner, T., de Abajo, F.J., et al., *Adaptive subwavelength control of nano-optical fields.* Nature, 2007. **446**(7133): p. 301-304.

105. Aeschlimann, M., Brixner, T., Cunovic, S., Fischer, A., Melchior, P., et al., *Nano-optical control of hot-spot field superenhancement on a corrugated silver*

surface. Ieee Journal of Selected Topics in Quantum Electronics, 2012. **18**(1): p. 275-282.

106. Tuchscherer, P., Rewitz, C., Voronine, D.V., de Abajo, F.J.G., Pfeiffer, W., et al., *Analytic coherent control of plasmon propagation in nanostructures.* Optics Express, 2009. **17**(16): p. 14235-14259.

107. Sonnichsen, C., Franzl, T., Wilk, T., von Plessen, G., Feldmann, J., et al., *Drastic reduction of plasmon damping in gold nanorods.* Physical Review Letters, 2002. **88**(7): p. 077402.

108. Nevels, R., Welch, G.R., Cremer, P.S., Hemmer, P., Phillips, T., et al., *Figuration and detection of single molecules.* Molecular Physics, 2012. **110**(15-16): p. 1993-2000.